A Preoptic Neurocircuit That Modulates Metabolic Flexibility

Julian M. Roessler[1,2,3,4], Matthew Alkire[1], Nathan Nigrin[1], Haorui Wang[1,5], Christopher M. Reid[1], Marissa D. Cortopassi[6], Millenia Waite[1], Brooke Linnehan[1], Eric C. Griffith[7], Mollie Madigan[8], Tenzin Kunchok[1], Alexander S. Banks[6], Fabian Schulte[1], Bukyung Kim[9], Bo-Yeon Kim[9], Jason K. Kim[9], Siniša Hrvatin[1,2,3,10,11*]

[1] Whitehead Institute for Biomedical Research; Cambridge, MA, USA

[2] Department of Biology, Massachusetts Institute of Technology; Cambridge, MA, USA

[3] Molecular and Cellular Neuroscience Program, Massachusetts Institute of Technology; Cambridge, MA, USA

[4]Laboratory for Mucosal Immunology, The Rockefeller University; New York, NY, USA

[5]Neuroscience Program, Columbia University; New York, NY, USA

[6] Division of Endocrinology, Diabetes, and Metabolism, Beth Israel Deaconess Medical Center and Harvard Medical School, Boston, MA, USA

[7]Department of Neurobiology, Harvard Medical School; Boston, MA, USA

[8] Department of Comparative Medicine, Massachusetts Institute of Technology; Cambridge, MA, USA

[9] Program in Molecular Medicine and Department of Medicine, Division of Endocrinology, Diabetes, and Metabolism, University of Massachusetts Chan Medical School; Worcester, MA, USA

[10]Department of Brain and Cognitive Sciences, Massachusetts Institute of Technology; Cambridge, MA, USA

[11] Howard Hughes Medical Institute, Massachusetts Institute of Technology, Cambridge, MA

*Correspondence: shrvatin@wi.mit.edu

Abstract

Precise, dynamic control of metabolic fuel usage in response to environmental challenges such as altered food availability or temperature change is essential for animal survival. In mammals, metabolic flexibility—the capacity to shift cellular metabolism between carbohydrate and fatty acid oxidation—is understood to be largely regulated by circulating hormones such as insulin and glucagon. However, the role of the central nervous system in coordinating fuel selection and tissue metabolic tuning remains underexplored. Here, we investigated the mechanisms that mediate metabolic reprogramming following the acute activation of torpor-associated glutamatergic Adcyap1+ torpor-regulating neurons in the anteroventral preoptic area ($avPOA^{Vglut2/PACAP}$). The activation of these neurons rapidly shifts whole-body fuel use from glucose to fatty acids, irrespective of fuel/food availability. This shift is associated with reduced glucose utilization stemming from the transient induction of selective insulin resistance in skeletal muscle. We find that this reduction in skeletal muscle glucose metabolism does not require direct muscle innervation but is rather mediated in part via corticosterone. In contrast to their activation, $avPOA^{Vglut2/PACAP}$ neuronal silencing results in improved glucose tolerance, demonstrating powerful bidirectional control of tissue-specific glucose metabolism, whole-body glucose levels, and fuel usage. Together, our findings uncover a novel POA -skeletal muscle pathway that dynamically controls glucose utilization and metabolic flexibility.

63 **Introduction**

64 Dynamic control of metabolism is essential for homeostatic maintenance in response to
65 changing environments, including altered temperature, food availability, and stress. For example,
66 in the context of nutrient deficit or increased energetic demands, fuel usage shifts from mixed
67 fatty acid and carbohydrate oxidation to near complete reliance on fat metabolism to preserve
68 glucose for use by the brain and prevent hypoglycemia[1,2]. Metabolic inflexibility, the inability to
69 efficiently switch between these fuel sources, has been linked to obesity, diabetes, and metabolic
70 disease[3,4].

71 Baseline regulation of blood sugar and fuel usage is largely controlled by the circulating
72 pancreatic hormones insulin and glucagon, with insulin resistance representing a key aspect of
73 disease-associated metabolic inflexibility[3–5]. While these hormonal regulators of metabolic
74 flexibility and their peripheral effectors have been extensively studied, less is known concerning
75 the role of the central nervous system (CNS) in dynamic top-down metabolic control. The
76 ventromedial hypothalamus (VMH) is the primary nucleus in the brain known to control
77 systemic glucose usage. Activation of counterregulatory steroidogenic factor 1 (SF-1)- or
78 Cholecystokinin B receptor (CCKBR)-expressing neurons in the VMH drives increased levels of
79 systemic glucose and peripheral tissue insulin sensitivity[6,7]. In addition, brain-body signaling via
80 the hypothalamic-pituitary-adrenal (HPA) axis has long been known to play a crucial role in
81 stress-induced metabolic responses, influencing insulin sensitivity and energy balance[8,9]. Yet,
82 which neuronal populations and brain-body axes mediate dynamic metabolic reprogramming in
83 response to various environmental challenges remain to be fully characterized.

84 In response to prolonged periods of food deprivation, a wide range of mammalian
85 species, including laboratory mice (*Mus musculus*), have evolved the capacity to suspend or
86 override canonical fasting metabolism to enter protective hypometabolic states such as daily
87 torpor and hibernation[10]. Fasting-induced daily torpor in mice is characterized by a reduction of
88 metabolic rate by approximately 60%[2,10] and an accompanying reduction in body temperature
89 from 37°C to near ambient levels. It has long been appreciated that entry into and maintenance of
90 these states requires utilization of internal fat stores as a primary energy source, shifting
91 metabolism almost entirely towards fatty acid oxidation[2]. Recent work from our group and others
92 has shown that torpor entry is centrally controlled by the activity of glutamatergic neurons within
93 the anteroventral preoptic area of the hypothalamus (avPOA^{Vglut2} neurons). The activation of this

94 neuronal population results in a dramatic reduction in energy expenditure even in the absence of
95 caloric restriction, suggesting that these neurons are powerful modulators of systemic metabolic
96 flexibility [11,12,13]. Discrete activation of this circuit thus provides a means to dissect a central
97 pathway for controlling metabolic flexibility, without the confounding metabolic effects of
98 prolonged fasting.

99 Here, we leverage the power of targeted opto- and chemogenetic circuit manipulation to
100 probe the metabolic effects of avPOA^{Vglut2} neuronal activation in the mouse and trace
101 downstream consequences for peripheral organ-specific glucose regulation. We show that
102 avPOA^{Vglut2} neuronal activation drives a preferential reduction in whole-body glucose
103 metabolism and a shift to a fatty acid oxidative state stemming from acute tissue-specific skeletal
104 muscle and brown adipose tissue insulin resistance. Moreover, acute inhibition of this population
105 improves glucose tolerance, nominating avPOA^{Vglut2} neurons as powerful bidirectional regulators
106 of glucose homeostasis. The resulting reduction in skeletal muscle glucose uptake and systemic
107 glucose intolerance is not dependent on the decrease in core body temperature, nor direct muscle
108 innervation, but rather is hormonally driven by the adrenal gland secretion of corticosterone.
109 Furthermore, these effects are recapitulated by the Adcyap1^{+} (PACAP-expressing) subpopulation
110 of avPOA^{Vglut2} neurons. Together, these findings identify avPOA^{Vglut2} neurons as a significant
111 unappreciated CNS glucoregulatory population intimately involved in the regulation of the
112 overall metabolic state. Targeted manipulation of this neuronal population and its downstream
113 effectors may thus prove relevant to the amelioration of disorders of metabolic inflexibility, such
114 as obesity, diabetes, and metabolic syndrome.
115

116 **Results**

117 **avPOA^{Vglut2} neurons control systemic metabolic fuel usage independent of changes in body**
118 **temperature**

119 Torpor is canonically understood as a strategy for energetic conservation during times of
120 nutrient deprivation[2]. While it is well-appreciated that fasting induces a shift from carbohydrate
121 oxidation (CHO) to fatty acid oxidation (FAO)[14], how torpor entry affects CHO versus FAO
122 utilization relative to surrounding periods of fasting at euthermic body temperatures remains less
123 well characterized. To monitor shifting fuel usage during fasting-induced torpor, 8-week-old
124 wild-type C57Bl/6J mice were implanted intraperitoneally with telemetric temperature probes,

125 fasted in metabolic cages for 24 hours, and monitored for changes in body temperature (T_b), gas
126 exchange, and respiratory exchange ratio (RER) — an established measure of CHO versus FAO
127 utilization (**Figure 1a)**. RER levels were found to decrease substantially during periods of torpor
128 relative to the fed state and surrounding periods of euthermic fasting (**Figure 1a, b)**, consistent
129 with an acute shift away from CHO and towards FAO during torpor.
130 We previously demonstrated that chemogenetic stimulation of avPOA neurons
131 phenocopies the decreased T_b and metabolic rate observed during natural torpor, thereby
132 providing a model to decouple avPOA neuronal activity from fasting-induced metabolic
133 changes[11]. To determine the metabolic consequences of avPOA neuronal activation, we
134 stereotactically introduced a neuronally targeted adeno-associated virus (AAV) expressing Gq-
135 DREADD[15] (AAV-hSyn-hM3D(Gq)-mCherry) into the avPOA of C57Bl/6J mice (**Figure 1c**).
136 The Gq-DREADD-activating ligand Clozapine-N-Oxide (CNO) was administered
137 intraperitoneally to these non-fasted animals, resulting in substantial decreases in both body
138 temperature and metabolic rate following CNO injection as compared to saline-injected control
139 animals (**Figures 1d-e, Supplementary Figures 1a,b**). These decreases were accompanied by
140 dramatic reductions in other metabolic parameters, including food intake, VCO_2, and VO_2
141 (**Supplementary Figures 1b-f**), as well as a marked shift in RER, from 0.86±0.01 to 0.66±0.02
142 (**Figure 1d**), consistent with a shift in metabolic fuel usage from mixed metabolism
143 (carbohydrate and fat) to primarily fat catabolism[3,16]. Moreover, utilizing the method of Frayn[16]
144 to quantify the relative contribution of CHO and FAO to overall energy expenditure, we
145 confirmed that upon avPOA stimulation animals transition from a mixed fuel state to nearly
146 exclusively using FAO for energy generation (**Figure 1g**). Together, these results demonstrate
147 that avPOA^{Vglut2} neuronal activation alone is sufficient to induce the alterations in fuel usage,
148 independent of caloric deprivation.
149 To determine whether the observed Gq-DREADD-driven RER effect was mediated by
150 decreased T_b, we increased the ambient temperature (T_a) from 24°C to 32°C, reasoning that
151 increased T_a would prevent the T_b decrease accompanying avPOA^{Vglut2} neuron activation.
152 Indeed, we observed that the average T_b of CNO-stimulated animals at this elevated ambient
153 temperature was 35.7±0.24°C as compared with 29.8±0.22°C when stimulated at T_a = 24°C
154 (**Figure 1h, Supplementary Figure 1e**). Strikingly, despite the absence of a large T_b drop,
155 stimulated animals exhibited a dramatic decrease in RER nearly identical to that observed at

156 24°C (**Figure 1h**), indicating that the observed metabolic shift is not a secondary consequence of
157 T_b reduction.
158
159 **avPOA^{Vglut2} neurons regulate blood glucose homeostasis and drive metabolic inflexibility**
160 To gain deeper insight into the metabolic consequences of avPOA neuronal stimulation,
161 we performed polar serum metabolomics analyses to identify changes in circulating metabolites
162 accompanying avPOA stimulation. Having previously identified glutamatergic avPOA
163 (avPOA^{Vglut2}) neurons as the primary drivers of torpid hypometabolism, we sought to target this
164 neuronal population more specifically. To this end, we transduced the avPOA of telemetric
165 probe-implanted *Vglut2-IRES-Cre* animals with AAV expressing either a Cre-dependent Gq-
166 DREADD or mCherry control. After collecting tail blood to establish a baseline for comparison,
167 animals were administered CNO, and blood samples were collected 15, 30, 60, and 120 minutes
168 post-injection, while continuously measuring T_b. We then performed plasma separation and polar
169 metabolome analysis on these samples, examining longitudinal changes in the abundance of
170 polar plasma metabolites in Gq-DREADD mice as compared with their mCherry counterparts
171 (**Figure 2a**). This analysis identified 4 significantly increased and 34 significantly decreased
172 polar plasma metabolites across all time points in avPOA^{Vglut2} neuron-stimulated animals
173 (**Figure 2b**). Observed changes involved significant decreases in key glycolytic and citric acid
174 cycle metabolites, including lactate, pyruvate, and 3-phosphoglycerate, accompanied by
175 increases in beta-hydroxybutyrate (**Figure 2b, Supplementary Figures 2a-d**). These changes
176 were monotonic across the duration of the experiment, suggesting continued suppression of
177 glucose metabolism (**Supplementary Figure 2a**), and were consistent with a state in which low
178 blood glucose levels lead to decreased glycolysis and a compensatory increase in FAO.
179 However, instead of a decrease in blood glucose levels, we observed an increase in serum
180 glucose (**Figure 2a**), suggesting that avPOA^{Vglut2} stimulation suppresses glucose metabolism
181 downstream of glucose availability. This suppression of glucose metabolism generates a
182 metabolically inflexible state, wherein animals rely nearly completely on fatty acid oxidation for
183 energy production.
184 Blood glucose levels are dynamically regulated by balancing glucose production through
185 hepatic gluconeogenesis and glycogenolysis with tissue glucose uptake via insulin-independent
186 and -responsive glucose transporters[17,18]. To test whether avPOA^{Vglut2} neuron stimulation resulted

187 in reduced glucose uptake, we subjected control (mCherry-injected) and experimental (Gq-
188 DREADD-injected) animals to a modified glucose tolerance test (GTT) following CNO
189 stimulation. Briefly, animals were fasted for 3 hours, administered CNO, and injected
190 intraperitoneally with a bolus of glucose (2 g/kg) 1 hour post-CNO stimulation (**Figure 2c**).
191 Strikingly, avPOA^{Vglut2} neuron-stimulated animals were significantly hyperglycemic at the end of
192 the test relative to their control counterparts (**Figures 2d-f**), indicating that avPOA^{Vglut2} neuron
193 stimulation induces pronounced systemic glucose intolerance. Consistent with our previously
194 observed effects on RER (**Figure 1f**), this glucose intolerance effect was not dependent on
195 decreased body temperature, as raising the ambient temperature (T_a = 32°C) failed to restore
196 glucose tolerance in these torpid mice (**Figure 2e-f**).
197 This finding led us to hypothesize that the effect of these neurons could be bidirectional,
198 and that inhibition of these neurons may improve glucose tolerance. To test this idea, we
199 transduced *Vglut2-IRES-Cre* animals with a Cre-dependent inhibitory Gi-DREADD (AAV-
200 hSyn-DIO-hM4D(Gi)-mCherry). To confirm effective targeting, we fasted Gi-DREADD-
201 transduced animals and observed that, as expected, upon CNO administration, Gi-DREADD-
202 mediated silencing of avPOA^{Vglut2} neurons was sufficient to prevent torpor entry
203 (**Supplementary Figures 2e, f**). To investigate the effects of avPOA^{Vglut2} neuronal silencing on
204 glucose tolerance, we first performed a baseline GTT in which mice were pretreated with PBS
205 and after one week of recovery, the same animals were pretreated with CNO and administered a
206 second GTT. Remarkably, acute inhibition of avPOA^{Vglut2} neurons resulted in increased glucose
207 tolerance, as peak glucose levels were significantly lower following CNO injection as compared
208 to PBS (PBS $Glucose_{Max}$ = 361.7 ± 11.4 mg/dL, CNO $Glucose_{Max}$ = 296.9 ± 12.4 mg/dL), and
209 remained consistently lower throughout the duration of the assay (**Figures 2h, i**). These findings
210 suggest that avPOA^{Vglut2} neuronal activity can bidirectionally control systemic glucose tolerance.
211 To examine the kinetics of this induced glucose intolerance, we transduced the avPOA of
212 *Vglut2-IRES-Cre* mice with AAV expressing either a Cre-dependent Channelrhodhopsin-2
213 (ChR2) (AAV-DIO-ChR2(H134R)-EYFP) or an EYFP (AAV-DIO-EYFP) control, and
214 subsequently implanted an optic fiber above the avPOA (**Figure 2j**). After surgical recovery, we
215 monitored plasma glucose and T_b over the course of 40 minutes of optogenetic blue light
216 stimulation (16 Hz, 8.5 mW, 1s on 1s off) as well as for an additional 40 minutes post-
217 stimulation. Optogenetic stimulation of avPOA^{Vglut2} neurons resulted in the anticipated decrease

218 in body temperature, as well as a rapid, monotonic increase in blood glucose not observed in the
219 EYFP controls (**Figures 2k-l, Supplementary Figure 2f**). Notably, upon light cessation, blood
220 glucose levels and T_b rapidly returned to normal, demonstrating that glucose intolerance is a
221 rapid, transient, and reversible effect of avPOA^{Vglut2} neuronal stimulation. Together, our findings
222 identify avPOA^{Vglut2} neurons as a significant glucoregulatory population that contributes to rapid,
223 reversible modulation of glucose homeostasis, drives a torpor-associated metabolic shift from
224 glucose metabolism towards fatty acid catabolism upon stimulation, and bidirectionally regulates
225 glucose tolerance upon activation or inhibition.
226
227 **avPOA^{Vglut2} neuronal activation drives insulin resistance and reduces glucose uptake**
228 Dysregulation of glucose homeostasis is often secondary to either reduced insulin
229 secretion or reduced insulin action on peripheral tissues in response to glucose challenge[17]. To
230 test whether the observed avPOA^{Vglut2} neuron-induced dysregulation of glucose clearance was a
231 consequence of reduced insulin secretion, we assessed circulating insulin levels in the context of
232 our GTT experimental paradigm. Remarkably, we observed no significant differences in insulin
233 levels in CNO-stimulated Gq-DREADD-expressing animals relative to mCherry controls
234 (**Supplementary Figure 3a**), suggesting that glucose-stimulated insulin secretion (GSIS) is
235 unaffected by avPOA^{Vglut2} neuronal stimulation. These findings were further confirmed by
236 monitoring GSIS in both Gq-DREADD-expressing and control mice in the context of a
237 hyperglycemic clamp[19] (**Supplementary Figure 3b**). Indeed, even the elevated insulin levels
238 observed in Gq-DREADD-expressing mice could not normalize plasma glucose in these animals
239 following CNO-stimulation, suggesting that avPOA^{Vglut2} neuron stimulation induces systemic
240 insulin insensitivity.
241 To further investigate this avPOA^{Vglut2} neuronal stimulation-induced insulin insensitivity,
242 we performed hyperinsulinemic-euglycemic clamp studies in Gq-DREADD-expressing *Vglut2-*
243 *IRES-Cre* mice and corresponding mCherry control animals following CNO stimulation (**Figure**
244 **3a**). Briefly, in both Gq-DREADD- and mCherry-expressing animals, we induced
245 hyperinsulinemia via constant insulin infusion while concomitant glucose infusion at a variable
246 rate was used to maintain euglycemia[20]. Importantly, all animals were partially restrained during
247 these studies for the purposes of blood sampling. This afforded us an ability to control for the

248 reduced locomotor activity of avPOA^{Vglut2} neuron-stimulated mice as compared to their
249 unstimulated control counterparts (see **Methods**).
250 Although euglycemia was achieved in both the Gq-DREADD-expressing and control
251 cohorts, the glucose-infusion rate (GIR) to maintain euglycemia during the insulin clamp
252 experiments in Gq-DREADD-expressing animals was significantly lower than that of controls,
253 indicating reduced insulin sensitivity (**Figures 3b, c)**. Moreover, while hepatic glucose
254 production during the insulin clamp was unaffected by avPOA^{Vglut2} neuronal stimulation, both
255 whole-body glucose turnover and glycolysis were dramatically reduced (**Supplementary**
256 **Figures 3f-i**), consistent with our observed metabolomics results in which circulating glycolytic
257 and TCA cycle metabolites were reduced by avPOA^{Vglut2} neuron stimulation. Taken together, our
258 findings show that avPOA^{Vglut2} neuronal activation induces systemic insulin resistance in mice,
259 thereby contributing to reduced glucose metabolism in these animals.
260
261 **avPOA^{Vglut2} neurons control organ-specific changes in glucose uptake**
262 To characterize the individual organs responsible for systemic insulin resistance, a bolus
263 of the non-metabolizable glucose analogue, ^{14}C-2-deoxy-glucose (^{14}C-2DG), was intraperitonelly
264 injected during the hyperinsulinemic-euglycemic clamp experiments. At the conclusion of the
265 experiments, animals were sacrificed, and liver, brain, white adipose tissue (WAT), brown
266 adipose tissue (BAT), heart, and gastrocnemius muscle were collected for biochemical analysis
267 of their ^{14}C-2DG-6-phosphate content. Scintillation counting revealed no significant changes in
268 the insulin-stimulated glucose uptake rate of heart, WAT, and brain. However, there was a
269 marked reduction in glucose uptake in both gastrocnemius muscle and BAT from avPOA^{Vglut2}
270 neuron-stimulated animals (**Figures 3d, e**), indicating organ-specific changes in insulin action
271 and glucose metabolism.
272 We calculated total glucose uptake in the presence or absence of avPOA^{Vglut2} neuronal
273 stimulation for each of the six tested tissues based on our measured rates of glucose uptake and
274 tissue weights. Consistent with prior findings that skeletal muscle accounts for ~80% of post-
275 prandial glucose utilization, and up to 75% of glucose disposal upon infusion[21], this analysis
276 revealed that diminished skeletal muscle glucose uptake accounts for a large fraction of the total
277 glucose utilization deficit observed in avPOA^{Vglut2} neuron-stimulated animals (**Figure 3f**),
278 suggesting that effects on skeletal muscle are the major contributor to the avPOA^{Vglut2} neuron-

279 driven impairment of insulin sensitivity. Importantly, we confirmed that this decrease in skeletal
280 muscle glucose uptake was not dependent on body temperature changes (**Figures 4a, b**). In
281 addition, comparative phospho-proteomic analysis of gastrocnemius samples from avPOA^{Vglut2}
282 neuron-stimulated and control animals provided evidence of avPOA^{Vglut2} neuron-driven
283 suppression of skeletal muscle insulin signaling (**Supplementary Figure 4c-f**). Given these
284 findings, we focused our subsequent investigation of the peripheral effects of avPOA^{Vglut2} neuron
285 activation on skeletal muscle.
286
287 **avPOA^{Vglut2} neuronal control of muscle glucose uptake occurs independent of muscle**
288 **innervation**
289 We next sought to determine the manner by which avPOA^{Vglut2} neurons convey
290 glucoregulatory signals to the periphery (**Figure 4a**). In this regard, skeletal muscle is innervated
291 by both sympathetic nervous system (SNS) and motor nervous system (MNS) fibers[22], and
292 sympathetic activation has been previously shown to enhance skeletal muscle glucose uptake via
293 the β-adrenergic signaling, primarily through β2-adrenergic receptors[23]. We therefore employed
294 a genetic approach to test the requirement for β-adrenergic sympathetic signaling in avPOA^{Vglut2}
295 neuron-driven changes in glucose tolerance, utilizing mice lacking β_1- and β_2-adrenergic
296 receptors ($\beta_{1/2}$-KO). For these studies, a *CaMKIIa* promoter-driven AAV (AAV-CaMKIIa-
297 hM3D(Gq)-mCherry) was used to achieve selective Gq-DREADD expression in excitatory
298 avPOA neurons of $\beta_{1/2}$-KO and wild-type control mice. To ensure that our results with this
299 *CaMKIIa* approach were consistent with our *Vglut2-IRES-Cre* experiments, we compared
300 expression patterns and GTT results of *CaMKIIα*-Gq-injected animals with those of Cre-
301 dependent *Vglut2-IRES-Cre* animals and found no significant differences in expression nor
302 glucose intolerance between cohorts (**Supplementary Figure 4g**). Following CNO stimulation,
303 we performed a GTT assay on these animals, which revealed no significant differences in CNO-
304 stimulated glucose intolerance between Gq-DREADD-expressing $\beta_{1/2}$-KO and wild-type animals
305 (**Figure 4c**), suggesting that $\beta_{1/2}$ adrenergic receptors were not required for avPOA^{Vglut2}
306 glucoregulatory signaling. As an orthogonal approach, we also performed chemical sympathetic
307 inhibition in Gq-DREADD-expressing *Vglut2-IRES-Cre* mice via the sympatholytic drug
308 guanethidine, which enters noradrenergic terminals and displaces norepinephrine from synaptic
309 vesicles to suppress norepinephrine release[24]. As expected, given its vasodilatory properties,

310 guanethidine treatment alone increased baseline glucose tolerance compared with PBS.
311 However, despite SNS inhibition by guanethidine, avPOA^{Vglut2} activation still induced glucose
312 intolerance (**Figure 4d**). Taken together, these genetic and pharmacological studies strongly
313 suggest that SNS activity is dispensable for avPOA^{Vglut2} neuron-driven glucose intolerance.
314 Motor innervation and movement also serve as well-appreciated regulators of glucose
315 metabolism[18]. To test the role of motor innervation on glucose uptake during avPOA^{Vglut2}
316 neuronal stimulation, we performed unilateral sciatic nerve denervations in mCherry control and
317 Gq-DREADD-transduced *Vglut2-IRES-Cre* mice[25]. This approach allowed us to compare, within
318 the same animal, the effects of avPOA^{Vglut2} neuron stimulation on muscle glucose uptake in the
319 innervated and the denervated limb (**Figure 4e**). Unilaterally denervated animals were injected
320 with CNO 1 hour prior to administration of the nonmetabolizable radioactive glucose analog ^{3}H-
321 2-Deoxyglucose. The animals were then monitored for changes in blood glucose and radioactive
322 substrate availability for 30 minutes, sacrificed, and their ipsi- and contra-lateral gastrocnemius
323 muscles processed for scintillation counting of ^{3}H-2-DG-6-Phosphate. As expected, denervated
324 gastrocnemius muscle exhibited reduced glucose uptake relative to the contralateral innervated
325 muscle under basal conditions (**Figure 4f**). Importantly, both innervated and denervated muscles
326 exhibited similarly pronounced reductions in glucose uptake following CNO-mediated
327 avPOA^{Vglut2} neuronal stimulation, with no significant differences in the ratio of CNO-stimulated
328 to baseline glucose uptake in the innervated and denervated muscle (**Figure 4f**). Taken together,
329 these results demonstrate that sympathetic innervation and direct motor innervation are
330 dispensable for avPOA^{Vglut2} neuron-driven changes in muscle glucose uptake.
331
332 **Corticosterone contributes to the avPOA^{Vglut2}-induced reduction of muscle glucose uptake**
333 Given the apparent dispensability of direct muscle innervation for avPOA^{Vglut2} neuron-to-
334 skeletal muscle signaling, we examined the potential involvement of known circulating
335 glucoregulatory hormones, assessing insulin, glucagon, leptin, and corticosterone plasma levels
336 in Gq-DREADD- and mCherry-transduced animals by ELISA following treatment with CNO
337 (**Figure 5a**). While no significant differences in insulin, glucagon, or leptin levels were
338 associated with avPOA^{Vglut2} neuronal stimulation (**Figure 5a**), we observed a ~2.5-fold increase
339 in plasma corticosterone levels in Gq-DREADD-expressing animals up to 2 hours post-CNO
340 stimulation, as compared with baseline (**Figure 5a**). The increase in corticosterone tracked well

341 with the observed increase in glucose levels (**Figure 5b**), suggesting a potential role for
342 circulating corticosterone levels in avPOA^{Vglut2} neuron-induced glucose uptake changes.
343 To directly test the contribution of corticosterone to avPOA^{Vglut2} neuron-induced glucose
344 intolerance, we utilized metyrapone, an inhibitor of corticosterone synthesis (**Figure 5c**)[26].
345 Baseline blood samples from unstimulated Gq-DREADD-expressing *Vglut2-IRES-Cre* mice
346 confirmed that metyrapone administration significantly decreased serum corticosterone levels
347 relative to saline-treated controls (**Figure 5d**). Subsequent GTT assays showed that metyrapone
348 treatment significantly attenuated CNO-induced glucose intolerance in Gq-DREADD-expressing
349 animals (**Figures 5e**). Although incomplete, this reversal of glucose intolerance in metyrapone-
350 treated animals identifies adrenal-derived corticosterone as a major regulator of glucose
351 homeostasis downstream of avPOA^{Vglut2} neuronal activation.
352
353 **avPOA^{PACAP} neuronal activity is sufficient to drive avPOA glucoregulatory effects**
354 Having outlined this POA-to-muscle glucoregulatory signaling axis, we sought to better
355 define the neuronal population within the POA that underlies these glucoregulatory effects. To
356 begin to address this question, we performed axon terminal and monosynaptic anterograde
357 mapping of downstream avPOA^{Vglut2} target regions (**Figure 6a, Supplementary Figures 5a,**
358 **b**)[27]. Both mapping approaches revealed the dorsomedial hypothalamus (DMH) and Raphe
359 Pallidus (RPa) as densely innervated by avPOA^{Vglut2} neurons. These regions have been heavily
360 implicated in control of metabolic rate and thermogenesis[28,29]. To test their role in avPOA^{Vglut2}
361 neuron-driven regulation of glucose homeostasis, we optogenetically stimulated axonal terminals
362 of avPOA^{Vglut2} neurons transduced with Cre-dependent ChR2 in either the DMH or RPa and
363 analyzed the effects on blood glucose tolerance. Despite dense axonal labeling in the RPa,
364 stimulation of avPOA^{Vglut2} neuron terminals in this region failed to induce glucose intolerance
365 (**Figure 6c**). By contrast, stimulation of DMH-projecting neurons fully phenocopied the glucose
366 intolerance induced by avPOA soma stimulation (**Figure 6c**), indicating that excitatory
367 avPOA->DMH projections are sufficient to drive acute glucose intolerance.
368 In addition to the anatomical heterogeneity of its projections, the avPOA glutamatergic
369 neuronal population is comprised of molecularly diverse neuronal subpopulations that could
370 mediate distinct effects on physiology[30]. In this regard, we initially focused on Adcyap1
371 (PACAP)- and Leptin Receptor (LepR)-expressing neurons given the established involvement of

372 these two largely excitatory POA neuronal subpopulations in metabolic and thermoregulatory
373 programs[13,31]. Integrated analysis of our prior single-nucleus transcriptomic data[11], showed that
374 *Adcyap1*+ neurons largely constitute a subset of POA glutamatergic neurons present throughout
375 the anatomical length of the POA, whereas LepR+ neurons form a distinct but molecularly
376 overlapping population with *Adcyap1* neurons located primarily in the anterior portion of the
377 POA (**Figures 6d, e**). To determine whether chemogenetic stimulation of one or both of these
378 subpopulations was sufficient to give rise to avPOA^{Vglut2}-associated glucoregulatory effects, we
379 stereotactically introduced our Cre-dependent AAV expressing Gq-DREADD into the avPOA of
380 *Adcyap1-2A-Cre* (avPOA^{PACAP}) or *Lepr-IRES-Cre* (avPOA^{LepR}) animals. Subsequent
381 chemogenetic stimulation of both avPOA^{PACAP} and avPOA^{LepR} neurons fully phenocopied the
382 glucose intolerance observed upon avPOA^{Vglut2} neuronal stimulation (**Figures 6f-h**),
383 demonstrating that either avPOA^{PACAP} or avPOA^{LepR} neuronal stimulation is sufficient to give
384 rise to the glucoregulatory effects of the broader avPOA^{Vglut2} population.
385 Given these results implicating PACAP^{+} avPOA neurons in the regulation of blood
386 glucose homeostasis, we sought to demonstrate their importance in regulating organismal
387 metabolic flexibility. To this end, we repeated our prior polar metabolomics approach done in
388 *Vglut2-IRES-Cre* animals with *PACAP-2A-Cre* mice that were stereotactically transduced with
389 Cre-dependent mCherry or Gq-DREADD AAVs, and upon recovery subjecting these animals to
390 blood collection and metabolic profiling following CNO stimulation. Consistent with the results
391 observed under avPOA^{Vglut2} neuronal stimulation, we observed significant decreases in the
392 abundance of major glycolytic and citric acid cycle metabolites when comparing avPOA^{PACAP}
393 Gq-DREADD-stimulated and control avPOA^{mCherry} animals 120 minutes after CNO
394 administration, including pyruvate, citrate, succinate, lactate, and malate (**Figure 6i**). Moreover,
395 consistent with increased reliance on fatty acid oxidation for fuel, we observed significant
396 increases in β-hydroxybutyrate in Gq-DREADD-stimulated avPOA^{PACAP} animals. There was
397 also a modest but non-significant increase in glucose abundance in these same animals 120
398 minutes post-stimulation. Analysis of earlier time points revealed a significant increase in blood
399 glucose in Gq-DREADD- vs. mCherry-expressing avPOA^{PACAP} animals at the 60-minute time
400 point (**Supplementary Figures 5d, e**), consistent both with our results in *Vglut2-IRES-Cre*
401 animals and a model in which avPOA^{PACAP} neurons directly regulate glucose tolerance. Finally,
402 we observed significant increases in the abundance of palmitate and α-lipoic acid at this time

403 point, indicating an increased mobilization of fat reserves to provide fuel via FAO during
404 avPOA^{PACAP} neuron stimulation. These results, coupled with our previous metabolomics
405 experiments in *Vglut2-IRES-Cre* animals, confirm that avPOA^{Vglut2} neurons are powerful
406 regulators of metabolic flexibility, and that avPOA^{PACAP} neurons are a Vglut2^{+} subtype sufficient
407 to drive this metabolic switch from carbohydrate to fatty acid catabolism.
408

409 **Discussion**

410 The ability to dynamically switch between metabolic fuel sources in the face of changing
411 nutrient availability and energetic demands is an essential feature of metabolic regulation.
412 Classically, this metabolic flexibility was understood to be driven mainly by circulating
413 hormonal factors, such as insulin and glucagon, with less known regarding the role of the central
414 nervous system in the control of whole-body and organ-specific fuel usage. Here, we focus on a
415 population of neurons associated with torpor and heat-defense to probe the mechanisms by
416 which CNS signals drive rapid systemic metabolic reprogramming in response to environmental
417 challenge. Surprisingly, we find that avPOA^{Vglut2} neuronal activation not only regulates whole-
418 body metabolic flexibility, but also controls fuel uptake and catabolism in an organ-specific
419 manner. Through a variety of interventions, we show that these effects are mediated via the
420 induction of acute insulin insensitivity in skeletal muscle and brown adipose tissue. In skeletal
421 muscle, this effect does not require sympathetic nervous system or motor neuron input. Rather,
422 the glucoregulatory effects of avPOA^{Vglut2} neurons appear to be mediated, at least in part by
423 corticosterone. Strikingly, acute silencing of this avPOA^{Vglut2} population was also found to
424 improve glucose tolerance, demonstrating that these neurons exert bidirectional control over
425 systemic glucose homeostasis and metabolic flexibility. While circuits regulating glucose
426 homeostasis and the counter-regulatory response to fasting have been described in other brain
427 regions[6,7,32], it is notable that the effects of avPOA^{Vglut2} activation and silencing on plasma
428 glucose levels exceed those of other known glucoregulatory circuits, suggesting that avPOA^{Vglut2}
429 neurons may be among the most potent central regulators of glucose homeostasis identified to
430 date.

431 Torpor is the primary physiological paradigm in which avPOA^{Vglut2} neuron function has
432 been described, and represents a dramatic challenge to normal thermal and metabolic
433 homeostasis[11,12]. In addition to their glucoregulatory capacities, activation of these neurons

434 results in profound hypothermia and hypometabolism, which are understood to be protective
435 adaptations for organismal survival[2]. One core aspect of this hypometabolism has been
436 hypothesized to be the preservation of glucose for the brain via reduction in peripheral organ
437 glucose uptake. However, until recently, it was unclear whether these neurons played an active
438 role in shaping specific, regulated aspects of this hypometabolic state, or if torpid metabolism
439 was secondary to decreases in T_b. Notably, a recent study examining a molecularly distinct
440 subpopulation of avPOA^{Vglut2} neurons expressing the neuropeptide QRFP (avPOA^{QRFP} neurons)
441 found that activation of this subpopulation results in both torpor-induction and impaired
442 glucoregulation, similar to avPOA^{Vglut2} neurons described in this work[33]. However, unlike our
443 findings, the researchers reported that avPOA^{QRFP} glucoregulation is secondary to body
444 temperature decreases. Our work shows that this is not a general principle of avPOA^{Vglut2}
445 neuron-mediated glucoregulation. Metabolic cage, GTT, and tissue-specific glucose uptake
446 experiments performed at elevated T_a, where animal T_b minimally decreases during avPOA^{Vglut2}
447 neuronal stimulation, all failed to ameliorate the observed glucose intolerance and uptake
448 defects. These divergent results suggest that there may be distinct subpopulations of avPOA^{Vglut2}
449 neurons which have temperature-dependent and -independent effects on glucose homeostasis.
450 Our data suggest a model in which activation of avPOA$^{Vglut2/PACAP}$ neurons contributes to
451 the reduction of glucose uptake in two of the primary consumers of glucose – skeletal muscle
452 and brown adipose tissue – thereby conserving glucose for uptake by the brain. Reduction of
453 glucose uptake in these tissues, coupled with peripheral reliance on fat stores and ketone bodies,
454 may allow for the stabilization of glucose levels such that the animal has sufficient available
455 energy stores to forage for food upon exit from torpor. While our results agree with studies of
456 overnight fasting that demonstrate relative insulin resistance and glucose intolerance compared
457 to mice with ad-libitum access to food[34], several glucoregulatory modalities (including changes
458 to insulin and glucagon levels) regulate glucose levels during fasting. Thus, further studies will
459 be needed to better understand the physiological benefit of avPOA$^{Vglut2/PACAP}$-mediated
460 glucoregulation during torpor. Moreover, avPOA^{PACAP} neurons have been implicated in
461 glucoregulation during warm challenge[35], and are involved in diverse behaviors, including sleep,
462 thirst, and cold-defense[31-37]. Future studies should examine the extent to which these neurons
463 regulate metabolic flexibility across these diverse physiological states.

464 An interesting aspect unaddressed by this study is what sensory modalities serve to
465 engage the activity of these neurons. Do these neurons respond directly to changes in circulating
466 hormone levels or metabolite abundance to trigger glucoregulatory metabolic shifts? Are there
467 ascending interoceptive neurocircuits that signal whole-body or tissue-specific nutrient
468 requirements to avPOA$^{Vglut2/PACAP}$ neurons? Future studies will be required to determine the
469 extent to which the glucoregulatory effects of these neurons impact mouse physiology during
470 these and other phenomenologically diverse states, and which sensory modalities trigger their
471 activation.
472 Intriguingly, this hypothalamic circuitry is largely conserved in non-torpid mammals,
473 including humans. Indeed, activation of avPOA^{Vglut2} neurons has been shown to induce torpor-
474 like hypometabolic state in the rat, a non-torpid animal[12]. Moreover, single-cell profiling of
475 avPOA subpopulations in non-human primates, such as marmosets, has revealed the presence of
476 avPOA$^{Vglut2/PACAP}$ neurons in the preoptic area of these animals (**Supplementary Figure 6**)[38,39].
477 While the function of these neurons in marmoset thermo- and gluco-regulation remains
478 unexplored, the anatomical and molecular conservation of these neurons in the preoptic area
479 suggests that they could have similar roles in regulating marmoset metabolic flexibility and
480 metabolic homeostasis. In humans, metabolic inflexibility is primarily understood within
481 pathological states such as diabetes, obesity, and metabolic syndromes, in which desensitization
482 mechanisms render peripheral tissues unable to respond to physiological levels of
483 glucoregulatory hormones such as insulin and leptin[21,36]. However, our findings raise the
484 possibility that such metabolic states can also be initiated or augmented by top-down
485 hypothalamic signaling. Future investigation will determine whether systematic changes in the
486 activity of these circuits over time predispose individuals to these disorders and facilitate the
487 development of metabolic pathologies.
488
489 **Methods and Materials**
490 **Mice**
491 Animal experiments were approved by the National Institutes of Health, Massachusetts Institute
492 of Technology's Committee on Animal Care (CAC), and Beth Israel Deaconess Medical
493 Center's IACUC following ethical guidelines described in the US National Institutes of Health
494 Guide for the Care and Use of Laboratory Animals. For initial metabolic cage experiments, we

495 used adult (8-12-week-old) C57BL/6J mice (The Jackson Laboratory, Stock 000664). For
496 natural, chemogenetic, and optogenetic torpor experiments, we used 8-12-week-old *Vglut2-*
497 *IRES-Cre* (The Jackson Laboratory, Stock 028863), *Adcyap1-2A-Cre* (The Jackson Laboratory,
498 Stock 030155), and *Lepr-IRES-Cre* (The Jackson Laboratory, Strain 008320) mice. For
499 adrenergic necessity experiments, we utilized 8-12-week-old β1/β2-KO animals (The Jackson
500 Laboratory, Stock 003810). All mice were housed at 22°C under a standard 12 h light/dark cycle
501 until they were subjected to surgery, at which point they were housed under a reversed 12 h
502 light/dark cycle. Power analysis was used to predetermine sample size, where appropriate (e.g
503 radioactive glucose uptake as well as hyperinsulinemic-euglycemic clamp experiments). Mice
504 were randomly assigned to experimental groups before surgery. Where possible, investigators
505 were blinded during analysis.
506
507 **Telemetric monitoring of core body temperature and gross motor activity**
508 Mice were implanted abdominally with telemetric temperature and activity probes (Unified
509 Information Devices, UCT-2112). After at least four days of recovery, animals were singly
510 housed and recorded in standard cages placed onto a radiofrequency receiver platform (Unified
511 Information Devices, UID Mouse Matrix). Core body temperature and gross motor activity were
512 logged every 300 ms based on animal movement and averaged over either 1- or 5-minute
513 windows, as appropriate. Temperature data were collated and exported from the MouseMatrix
514 Software (Unified Information Devices, MouseMatrix 1.6.2) for downstream processing.
515 Analysis of temperature data was performed in R (R Core Team) using a custom-written R
516 Script.
517
518 **Metabolic cage experiments**
519 Metabolic cage data was collected on individually housed mice placed in a Promethion
520 indirect calorimeter (Sable Systems) with a temperature-controlled cabinet (Pol-Eco) and
521 provided with ad libitum food (Labdiet 5008) and water purified by reverse osmosis. Starr
522 Scientific telemetry receiver bases were placed beneath the Promethion Cages to match the
523 implanted probes. Mice were maintained under 12 h light/dark photoperiods (0600–1800) at an
524 ambient temperature of 23 ± 0.2°C. Position and physical activity were collected every second.

525 Rates of oxygen consumption (VO_2) and carbon dioxide production (VCO_2) were measured
526 every 2 min. Energy expenditure was calculated with the Weir equation[40].
527
528 **Fasting-inducted torpor**
529 Telemetric temperature probe-implanted adult (8-18-week-old) mice were singly housed before
530 the induction of torpor. Each mouse was moved to a new individual cage containing water and
531 nesting material but devoid of bedding and food at the beginning of the dark cycle (ZT 11.5).
532 Initial bouts of torpor were observed after approximately 8-12 h of fasting. Mice were returned to
533 their standard cages containing food 24 h after the start of the fast. The ambient temperature of
534 the facility was maintained at ~22°C.
535
536 **Stereotactic viral injection and fiber implantation**
537 For injections, mice were anaesthetized with 3% isoflurane and placed in a stereotaxic head
538 frame (Kopf Instrument, model 1900). Animals were kept constantly sedated using 1-1.5%
539 isoflurane, and either Buprenorphine SR (1.0 mg/kg) or Ethiqa SR (3.25 mg/kg) were
540 administered for analgesia. The skull was leveled in the AP and ML directions, and bore holes
541 were drilled using a stereotaxic drill (David Kopf Instruments). For chemogenetic experiments,
542 unless otherwise specified, craniotomies and viral administration were bilateral. For
543 optogenetics, craniotomies and viral administration were unilateral. An air-based injection
544 system built with Digital Manometer (Grainger, 9LHH8) was used to infuse the virus through
545 pulled glass capillaries. Virus was administered at the following coordinates - POA: AP +0.4
546 mm, ML ±0.5 mm, DV −5.02 mm, PVH: AP -1.0 mm, ML ±0.1 mm, DV −4.5mm, DMH: AP -
547 1.8 mm, ML ±0.5 mm, DV −5.02 mm, PAG: AP -3.25 mm, ML ±0..25 mm, DV −1.8 mm, RPa:
548 AP -5.5 mm, ML ±0.0 mm, DV −5.75 mm. Virus was infused at approximately 100 nL min^{-1},
549 and the needle was kept at the injection site for 10 min before withdrawal. Unless otherwise
550 specified, 100 nL of virus was administered per site (unilateral: 100 nL total, bilateral 200 nL
551 total). Following needle removal, the incision was closed using 4-0 monocryl adsorbable suture
552 (Ethicon) with alternating box knots in an interrupted pattern.
553 For optic fiber implantation for optogenetics, 400 μm, 0.37 NA borosilicate mono fiber
554 optic cannulae (Doric, MFC_400/430-0.37_###_MF1.25_FLT, where ### corresponds to fiber
555 length) were implanted approximately 500 μm above the injection site. Fibers were initially

556 fixed to the head using superglue (Gorilla Super Glue Gel), followed by Metabond (CB
557 Metabond S380) to ensure the stability of the implant. For optogenetics experiments, 100 nL of a
558 1:1 mixture of AAV8-hSyn-DIO-hM3D(Gq)–mCherry, or AAV8-hSyn-DIO-hM3D(Gq)–
559 mCherry and AAV8-EF1a-ChR2(H134R)-EYFP, respectively, were injected unilaterally into the
560 POA. Chemogenetic stimulation of POA neurons followed by monitoring of core temperature
561 decreases was used to validate injection accuracy. Animals not demonstrating temperature
562 reductions upon administration of CNO were removed from the analysis.
563
564 **Viral constructs**
565 AAV8-hSyn-DIO-hM3D(Gq)-mCherry (Addgene, 44361-AAV8), AAV-hSyn-fDIO-
566 hM3D(Gq)-mCherry-WPREpA (Addgene, 154868-AAV8), pAAV-EF1a-double floxed (DIO)-
567 hChR2(H134R)-EYFP-WPRE-HGHpA (Addgene, 20298-AAV1), pAAV-hSyn-DIO-
568 hM4D(Gi)-mCherry (Addgene, 44362-AAV8), AAV-CaMKIIa-hM3D(Gq)-mCherry (Addgene,
569 50476-AAV8), AAV-hSyn-hM3D(Gq)-mCherry (Addgene, 50474-AAV8), AAV-hSyn-DIO-
570 mCherry (Addgene, 50459-AAV8), and pAAV-hSyn-DIO-EGFP (Addgene, 50457-AAV8) were
571 obtained from Addgene. AAV-EF1a-DIO-EYFP (AAV2) was prepared by the UNC Viral Core.
572 AAV-DIO-TK-P2A-EGFP and HSV-H129-ΔTK-tdTomato were prepared by the University of
573 California Irvine Viral Core.
574 All AAV viruses were diluted with PBS to a final concentration between 5×10^{12} and $1 \times$
575 10^{13} genome copies per mL before stereotactic delivery into the mouse brain. HSV-H129-ΔTK-
576 tdTomato was administered at 5×10^{8} PFU per mL (100 nL unilaterally).
577
578 **Chemogenetic induction and inhibition of torpor**
579 *Induction*
580 Cre-expressing animals were bilaterally transduced with AAV8-hSyn-DIO-hM3D(Gq)-mCherry.
581 Gq-DREADD-transduced animals were implanted with telemetric temperature probes and
582 allowed to recover for a minimum of 5 days post-surgery. Following this recovery window,
583 animals were injected with CNO, and body temperature was monitored to confirm accuracy of
584 injection. Animals were considered to be torpid if their body temperatures decreased below 34°C
585 upon CNO administration.
586

587 CNO solution was prepared by initially dissolving CNO hydrochloride (Sigma-Aldrich,
588 SML2304) in H_2O to generate a stock solution of 5 mg/mL. The stock solution was diluted with
589 PBS to a final concentration of 0.2 mg/mL, and approximately 125 µL was injected
590 intraperitoneally per mouse for a final injection concentration of 1 mg kg^{-1} in bilaterally injected
591 animals. Unilaterally injected animals received concentrations of 2 mg kg^{-1}.
592
593 *Inhibition*
594 Cre-expressing animals were bilaterally transduced with AAV8-hSyn-DIO-hM4D(Gi)-mCherry.
595 Gi-DREADD-transduced animals were implanted with telemetric temperature probes and
596 allowed to recover for a minimum of 5 days post-surgery. Following this recovery window,
597 animals were first fasted overnight starting in the dark phase (ZT12-12). Animals were injected
598 with PBS at ZT22, right before the onset of the light phase, and body temperature was monitored
599 to confirm accuracy of injection. Animals were considered to be torpid if their body temperatures
600 decreased below 34°C. Animals were recovered for 7 days, and subjected to this fasting
601 paradigm again, except CNO (10 mg/kg) was injected at ZT22. Injections were considered
602 successful if animals entered torpor when injected with PBS, but did not when injected with
603 CNO. If entry into torpor was not inhibited by CNO the animals were excluded from further
604 experiments.
605
606 **Optogenetic stimulation of avPOA^{Vglut2} neurons**
607 Animals expressing either ChR2(H134R) or an EYFP control, and implanted with a fiber optic
608 cannula, were allowed to recover 5 days post-surgery before confirming proper injection location
609 via CNO stimulation. Animals that failed to demonstrate a body temperature decrease were
610 excluded from further analysis. After a 2-week post-surgery recovery period to allow for
611 adequate viral expression, awake, freely moving animals were tethered to a fiber optic patch cord
612 (Doric) and placed in a deep-well cage (WPI) with free access to food and water. Animals were
613 allowed to acclimate to the new environment for 1 h prior to the start of stimulation. To deliver
614 light pulses a PulsePal2 (SanWorks) was utilized as a pulse train generator, which was connected
615 to a desktop computer via USB and controlled via a custom Python script. Pulses from the
616 controller were conveyed via a 455 nm fiber-coupled LED (ThorLabs M455F3) connected to the
617 mouse via patch cords connected through a rotary joint (ThorLabs RJ1) to allow for

618 unencumbered movement of the animal. For ChR2 experiments, the stimulation paradigm was as
619 follows: 8.5 mW, 10 μs pulse, 50 μs interval (16 Hz), Duty Cycle 1s ON 1s OFF. Power output
620 was confirmed at the fiber tip via a power meter (ThorLabs PM100D) prior to each experiment.
621 For fasting experiments, such as GTT or overnight fasting, an identical setup was utilized, but
622 the animal was not given food (access to water was maintained).
623
624 Following the completion of optogenetic experiments, animals were sacrificed, perfused with 4%
625 PFA, and their brains were sectioned to confirm the accuracy of fiber placement.
626
627 **Intraperitoneal glucose tolerance tests (GTT)**
628 For chemogenetic glucose tolerance testing, Gq-DREADD or Gi-DREADD-expressing and
629 control animals were weighed and moved to a clean cage containing a bedding square and water,
630 but no food, prior to the beginning of the dark cycle (ZT 11.5), and placed onto telemetric
631 temperature platforms. After 3 hours of fasting and a "Pre-CNO" blood glucose reading (Bayer
632 Onetouch), animals were injected with 1 mg kg^{-1} CNO and returned to their cage for 60 minutes.
633 A baseline blood glucose reading was subsequently taken (t = 0), and animals were injected with
634 2 g/kg glucose (10*Body Weight 20% glucose). Blood glucose readings were then taken at 15,
635 30, 45, 60, 90, and 120 minutes post-glucose injection prior to returning animals to their home
636 cages.
637
638 For optogenetic glucose tolerance tests, ChR2(H134R)- or EYFP-expressing animals were
639 weighed and connected to a fiber optic patch cord and placed in a clean cage with a nesting
640 square and water but no food. Animals were fasted for 3 hours, sampled for blood, and injected
641 with a volumetrically equivalent amount of saline to CNO that would have been injected in a
642 chemogenetic GTT (i.e. 5 μL saline/g of mouse). After a 60-minute interval, a baseline blood
643 sample was taken, and animals were injected with 2 g/kg glucose. Immediately upon glucose
644 injection, blue light (455 nm) stimulation commenced. Blue light stimulation was continued
645 throughout the duration of the experiment, and blood was sampled at the time points previously
646 described. Blue light stimulation was terminated after t = 120 minutes, and animals were
647 disconnected and returned to their home cages.
648

649 Data were recorded, graphed, and analyzed in GraphPad Prism. AUC calculations were
650 performed using GraphPad Prism analytical tools.
651
652 **Radioactive glucose uptake**
653 *Radioactive glucose uptake assay*
654 Male 8-12-week-old *Vglut2-IRES-Cre* animals were transduced with either mCherry or Gq-
655 DREADD. After validating Gq-DREADD animals' ability to undergo chemogenetic topor,
656 animals were weighed, transferred to a new cage, and fasted for 3 hours. Animals were
657 administered CNO and allowed to equilibrate body temperature for 60 minutes, upon which time
658 initial blood glucose and scintillation counting samples were taken and animals were injected
659 with a mixture of 20 μCi 2-[1,2-^{3}H(N)]-Deoxy-D-glucose (^{3}H-2-DG), 0.5 U/kg Insulin, and 1
660 mM 2-Deoxy-Glucose as per Møller et al[41]. Animals were then placed in a new cage, and 3 μL
661 of blood were taken for scintillation counting along with 1 drop for blood glucose measurements
662 at 5, 10, 20, and 30 minutes post-injection. Blood collected for scintillation counting was added
663 to 5 mL of Opti-Fluor (Perkin-Elmer), mixed, and placed into a Perkin-Elmer Imager for
664 scintillation counting. Following 30-40 minutes of uptake, animals were euthanized, and their
665 gastrocnemius, soleus, and BAT were dissected and snap-frozen in liquid nitrogen. Scintillation
666 samples were measured for tritium over 1 minute, and plasma tritium concentration were
667 recorded as disintegrations per minute (DPM).
668
669 *Determination of tissue-specific glucose uptake rate*
670 To determine tissue-specific glucose uptake rate, we performed chromatographic
671 separation of ^{3}H-2-DG from ^{3}H-2-DG-6-Phosphate, based on a protocol developed by Kim et
672 al[20]. Using ^{3}H-2-DG-6-Phosphate as a proxy for tissue-specific uptake is predicated on the fact
673 that ^{3}H-2-DG is metabolized to ^{3}H-2-DG-6-Phosphate almost immediately upon entry into the
674 cell, which then precludes its exit from the tissue. Measurement of total ^{3}H-2-DG includes
675 interstitial, unmetabolized ^{3}H-2-DG, and is therefore susceptible to artefactual over- or under-
676 estimation of glucose uptake based on state-dependent differences in tissue perfusion. To avoid
677 this confound, we utilized Poly-Prep anion exchange columns (Bio-Rad, 731-6211) to isolate the
678 ^{3}H-2-DG-6-Phosphate. Briefly, tissues were weighed and homogenized in 10 volumes of sterile,
679 deionized water. Homogenized tissues were then heated to 95°C for 10 minutes, cooled to room

680 temperature, vortexed, and centrifuged for 10 minutes at 21430 RCF. Subsequently, 33.3 μL of
681 homogenate was added to 4.967 mL of Opti-Fluor for scintillation counting. During this time,
682 the Poly-Prep anion exchange column was equilibrated with 6 mL of sterile deionized water.
683 Following equilibration, 333 μL of homogenate was applied to the columns and allowed to flow
684 through by gravity. The column was subsequently washed 3 times with 2 mL of sterile,
685 deionized water, and the flowthrough was collected in scintillation vials as the "wash" fraction.
686 Finally, the ^{3}H-2-DG-6-Phosphate was eluted from the column using a 0.3 M Formic Acid/0.5 M
687 NH_4CH_3COO elution buffer. Elution was accomplished via 3 washes of 2 mL using the elution
688 buffer and collected in scintillation vials. The wash and elution (500 μL) were added to 5 mL of
689 Opti-Fluor, and the samples were vortexed and analyzed via scintillation counting.
690
691 For quantitation of tissue-specific glucose uptake rates, we employed a method modified
692 from Møller et al[41]. Briefly, the DPM of the eluate, representing the ^{3}H-2-DG-6-Phosphate
693 concentration in the tissue, was related to the time of uptake and weight of tissue to obtain a
694 DPM g^{-1} min^{-1} value, representing tissue-specific uptake rate. The time-weighted ^{3}H-2-DG
695 appearance was then extrapolated from the DPM of ^{3}H-2-DG in the blood and divided by the
696 time-weighted total glucose concentration to obtain the specific activity of ^{3}H-2-DG in the blood
697 (DPM/μmol). The glucose uptake index for the tissue was then calculated by dividing the tissue
698 uptake rate by the specific activity, and expressing this value as nmol g^{-1} min^{-1}.
699
700 **Immunoblotting**
701 Male, 8-12-week-old *Vglut2-IRES-Cre* animals validated to have body temperature drops and
702 glucose intolerance when stimulated with CNO were subdivided into three cohorts, injected with
703 either saline, CNO (1 mg/kg), or insulin (0.5 IU/kg), respectively, and monitored for blood
704 glucose changes over a 45-minute period. After 45 minutes, animals were sacrificed, and
705 gastrocnemius, soleus, quadriceps, liver, and BAT were dissected and snap-frozen. These tissues
706 were then homogenized in Radioimmunoprecipitation (RIPA) Buffer composed of 150 mM
707 NaCl, 1.0% (w/v) Triton X-100, 0.5% (w/v) Sodium Deoxycholate, 0.1% (w/v) sodium
708 dodecylsulfate, 50 mM Tris (pH 8), EDTA-free protease inhibitor (Roche), and PhosSTOP
709 phosphatase inhibitor (Roche), using a BioRuptor (Qiagen). Lysates were cleared by
710 centrifugation in a microcentrifuge (21430 RCF for 10 min at 4°C), and protein concentrations

711 were quantified using the Pierce BCA Protein Assay Kit (Thermo Fisher). Lysate samples were
712 prepared by the addition of 5× Laemelli Buffer (0.242 M Tris, 10% SDS, 25% glycerol, 0.5 M
713 dithiothreitol (DTT) and bromophenol blue), resolved by Bis-Tris SDS–PAGE, and analyzed by
714 immunoblotting. Antibodies and concentrations used for immunoblotting include Insulin
715 Receptor β (4B8) Rabbit mAb #3025 (Cell Signaling Technologies) 1:1000, Akt Antibody #9272
716 (Cell Signaling Technologies) 1:1000, and Phospho-Akt (Ser473) Antibody #9271 (Cell
717 Signaling Technologies) 1:500. Proteins were visualized using an Anti-rabbit IgG HRP-linked
718 Antibody #7074 (Cell Signaling Technologies) 1:3000 in combination with the
719 chemiluminescent Pierce™ ECL Western Blotting Substrate (ThermoFisher) using an X-OMAT
720 film processor.
721
722 **Sciatic nerve denervation**
723 Sciatic nerve denervation procedures were modeled on those described in Volodin et al[42].
724 Briefly, animals were anesthetized with 3% isoflurane and administered analgesics. The sciatic
725 nerve was then accessed via the back right flank of the animal and severed at both distal and
726 proximal ends, such that there was no reattachment of nerve fibers during the course of recovery.
727 Accuracy of the cut was validated via observation of the animal post-operation. Severing the
728 sciatic nerve causes a stereotyped dragging of the ipsilateral limb. Animals confirmed to have
729 successful denervations were included in experimental cohorts, whereas those that retained limb
730 mobility were excluded. Animals were allowed to recover for 72 hours prior to use in radioactive
731 glucose uptake assays previously described.
732 When dissecting organs for analysis of tissue-specific glucose uptake, both innervated
733 and denervated gastrocnemius muscles were harvested. These tissues were processed in an
734 identical manner, and the ratio of innervated:denervated glucose uptake was used as a metric for
735 the reduction in glucose uptake in the same animal that resulted from denervation.
736
737 **Blood collection**
738 Tail blood was collected from animals by opening a small hole in the tail of the animal
739 and manually extracting 20 μL of blood into a Lithium Heparin Microvette (Sarsdedt). For
740 longitudinal assays, no more than 150 μL of blood was removed from an animal. Following
741 blood extraction, microvettes were placed on ice for no longer than 60 minutes, and then

742 centrifuged in a microcentrifuge for 5 minutes at 2000 RCF to separate blood cells from plasma.
743 Plasma was extracted from these tubes, aliquoted, snap-frozen in liquid N_2, and placed at -80°C
744 for long-term storage.
745
746 **ELISA assays**
747 All assays were performed according to manufacturers' instructions, as briefly described below:
748 *Insulin*
749 Following plasma separation, 10 μL plasma from each mouse was used for the Mouse Ultra-
750 Sensitive ELISA Assay (Crystal Chem), plated in 5 μL duplicates. Samples were compared
751 against a standard curve and analyzed using a Spectramax iD3 plate reader with a reference
752 wavelength of 630 nm and a measured wavelength of 450 nm. Data were fit using a linear curve,
753 and cohort analysis was performed using two-tailed t-tests.
754 *Glucagon*
755 Following plasma separation, 20 μL plasma from each mouse was used for the Mouse Glucagon
756 ELISA Assay (Crystal Chem), plated in 10 μL duplicates. Samples were compared against a
757 standard curve and analyzed using a Spectramax iD3 plate reader with a reference wavelength of
758 630 nm and a measured wavelength of 450 nm. Data were fit using a 4-parameter logistic curve,
759 and cohort analysis was performed using two-tailed t-tests.
760 *Leptin*
761 Following plasma separation, 10 μL plasma from each mouse was used for the Mouse Leptin
762 ELISA Assay (Crystal Chem), plated in 5 μL duplicates. Samples were compared against a
763 standard curve and analyzed using a Spectramax iD3 plate reader with a reference wavelength of
764 630 nm and a measured wavelength of 450 nm. Data were fit using a 4-parameter logistic curve,
765 and cohort analysis was performed using two-tailed t-tests.
766 *Corticosterone*
767 Following plasma separation, 5 μL plasma from each mouse was used for the Corticosterone
768 ELISA Assay (Enzo Life Sciences). Samples were enriched for steroids using the provided
769 Steroid Displacement Reagent and plated in duplicate. Samples were compared against a
770 standard curve and analyzed using a Spectramax iD3 plate reader with a reference wavelength of
771 580 nm and a measured wavelength of 405 nm. Data were fit using a 4-parameter logistic curve,
772 and cohort analysis was performed using two-tailed t-tests.

773

774 **Polar serum metabolomics**

775 To begin, 10 μL aliquots of plasma from blood samples was combined with 90 μL of
776 75:25:0.2 acetonitrile:methanol:formic acid containing 0.2 μg/mL internal standards and
777 vortexed for 5 minutes as 4°C. Subsequently, the samples were spun at 21430 RCF for 10
778 minutes in a refrigerated centrifuge at 4°C. Supernatant was taken, and 15 μL was added to
779 LC/MS vials for analysis.

780 Analysis was conducted on a QExactive benchtop Orbitrap mass spectrometer equipped
781 with an Ion Max source and a HESI II probe, which was coupled to a Dionex UltiMate 3,000
782 UPLC system (Thermo Fisher Scientific). External mass calibration was performed using the
783 standard calibration mixture every 7 days. Chromatographic separation was achieved using the
784 following conditions: buffer A was 20 mM ammonium carbonate, 0.1% ammonium hydroxide;
785 buffer B was acetonitrile. The column oven and autosampler tray were held at 25°C and 4°C,
786 respectively. The chromatographic gradient was run at a flow rate of 0.150 mL min−1 as
787 follows: 0–20 min: linear gradient from 80% to 20% B; 20–20.5 min: linear gradient from 20%
788 to 80% B; 20.5–28 min: hold at 80% B. The mass spectrometer was operated in full-scan,
789 polarity switching mode with the spray voltage set to 3.0 kV, the heated capillary held at 275°C,
790 and the HESI probe held at 350°C. The sheath gas flow was set to 40 units, the auxiliary gas
791 flow was set to 15 units, and the sweep gas flow was set to 1 unit. The data acquisition was
792 performed over a range of 70–1,000 m/z, with the resolution set at 70,000, the automatic gain
793 control target at 10E6, and the maximum injection time at 20 ms. Relative quantitation of polar
794 metabolites was performed with TraceFinder 2.2 (Thermo Fisher Scientific) using a 5 p.p.m.
795 mass tolerance and referencing an in-house library of chemical standards.

796

797 **Hyperinsulinemic-euglycemic clamp**

798 Survival surgery, to place an indwelling intravenous catheter, was performed 5~6 days prior to
799 the insulin clamp experiments[20]. On the day of the euglycemic clamp experiment, mice were
800 placed in a rat restrainer with their tails tape-tethered at one end to minimize animal stress and
801 allow access to tail blood sampling during the experiment. Mice were allowed to acclimatize to
802 this state for 2 hours prior to the insulin infusion. During this 2-h acclimation period, D-[3-^{3}H]
803 glucose was infused (0.05 μCi/min) using a microdialysis pump to assess the basal rate of whole-

804 body glucose turnover (i.e, basal hepatic glucose production). Subsequently, a baseline blood
805 sample (60 μL) was collected for the measurement of basal plasma glucose, insulin, and [^{3}H]
806 glucose concentrations[20].
807 Following the basal period, a 2-h hyperinsulinemic-euglycemic clamp was conducted
808 with a primed (150 mU/kg body weight) and continuous infusion (2.5 mU/kg/min) of human
809 insulin to raise plasma insulin within a physiological range (approximately 300 pM)[20]. Blood
810 samples (10 μL) were collected at 10~20-minute intervals for the measurement of plasma
811 glucose levels. Based on plasma glucose levels, 20% glucose was infused at variable rates to
812 maintain euglycemia (~120 mg/dL) throughout the clamp. To determine insulin-stimulated
813 whole-body glucose turnover, continuous infusion of [3-^{3}H] glucose was applied throughout the
814 clamp (0.1 μCi/min). To estimate insulin-stimulated glucose uptake in individual organs, a bolus
815 of 2-deoxy-d-[1-^{14}C] glucose (2-[^{14}C]DG) (10 μCi) was administered at 75 min after the start of
816 the clamp[20]. Blood samples (10 μL) were taken at 80, 85, 90, 100, 110, and 120 min for the
817 measurement of plasma [^{3}H] glucose, ^3H_2O, and 2-[^{14}C] DG concentrations. A final blood
818 sample (20 μL) was taken at the end of the clamp to measure plasma insulin concentrations.
819 At the end of the insulin clamp, mice were anesthetized, and skeletal muscles (gastrocnemius and
820 quadriceps) from both hindlimbs, white and brown adipose tissues, liver, brain, and heart were
821 collected for biochemical analysis[20]. The tissues were rapidly frozen in liquid N_2, and stored at
822 −80°C until biochemical analysis was performed. Tissue-specific uptake was determined as
823 described in **Radioactive glucose uptake** above.
824
825 **Phosphoproteomics**
826 *Proteolytic digestion and peptide extraction*
827 Tissues were lysed at 70°C for 15 min in 1 mL 1X SDS lysis buffer (5 % (w/v) SDS, 100 mM
828 TEAB pH 8.5, 40 mM CAA, 10 mM TCEP, protease inhibitor cocktail, phosphatase inhibitor
829 cocktail) in Low Protein Binding Microcentrifuge Tubes (Thermo Scientific, Waltham, MA,
830 USA). Cellular debris was removed by centrifugation at 15,000 x g for 5 min. Protein (600 μg)
831 was purified via the SP3 method as in Hughes et al[43]. Proteins were bound to 120 μL SP3 beads
832 by adding 2.4 mL 100 % (v/v) ethanol followed by three washing steps with 1 mL 80 % (v/v)
833 ethanol. Samples were digested with trypsin/LysC mix (1:50) in 300 μL 100 mM TEAB, and
834 proteins were digested overnight in a shaking incubator at 37°C at 115 RPM. The following day,

835 an additional 6 µg trypsin/Lys-C mix was added in 6 µL 100 mM TEAB and the digestion
836 continued for 4 hours at 37°C. Peptide digests (240 µg) were dried in a speed-vac concentrator
837 and resuspended in 40 µL 100 mM TEAB. Peptides were labeled with 500 µg TMTpro label
838 resuspended in 20 µL anhydrous acetonitrile. TMTpro-labeled samples were quenched for 30
839 min at room temperature with 5 µL 5% hydroxylamine in 100 mM TEAB. Labeled peptides
840 were pooled together and desalted on a 500 mg C18 SepPak column (Waters, Milford, MA,
841 USA).
842 The TMTpro pooled sample was split, with one part used for proteome analysis and the other
843 part used for phosphopeptide enrichment. The proteome sample was fractionated using a Strong
844 Anion Exchange column (Thermo Scientific, Waltham, MA, USA). Increasing concentrations of
845 ammonium acetate (0, 20, 50, 100, 200, 500 mM) were used for elution. Low salt fractions (0,
846 20, 50 mM ammonium acetate) and high salt fractions (100, 200, 500 mM ammonium acetate)
847 were pooled, respectively, and lyophilized. The phosphopeptide sample was enriched using the
848 High Select™ TiO_2 phosphopeptide enrichment kit according to the manufacturer's instructions
849 (Thermo Scientific, Waltham, MA, USA). All TiO_2 flowthrough and wash fractions were
850 pooled, lyophilized, and further enriched using the High Select™ Fe-NTA phosphopeptide
851 enrichment kit according to the manufacturer's instructions (Thermo Scientific, Waltham, MA,
852 USA). The low salt and high salt proteome samples, as well as both phosphopeptide-enriched
853 samples, were then fractionated with the High pH Reversed-Phase Peptide Fractionation Kit
854 (Thermo Scientific, Waltham, MA, USA) using the following 12-step gradient of increasing
855 acetonitrile concentrations: 5, 7.5, 10, 12.5, 15, 17.5, 20, 22.5, 25, 27.5, 30, 60%. The following
856 fractions were then pooled together and lyophilized: 1+7, 2+8, 3+9, 4+10, 5+11, 6+12.
857 Lyophilized fractions were resuspended in 12 µL 0.2% formic acid in MS-grade water for LC-
858 MS analysis.
859 *LC-MS data collection:*
860 Mass spectrometry was performed using an Orbitrap Eclipse mass spectrometer equipped with a
861 FAIMS Pro source, connected to a Vanquish Neo nLC chromatography system using an
862 EasySpray ES902 column (75 µm x 25 cm, 100 Å), all from Thermo Fisher Scientific (Waltham,
863 MA, USA). Peptides were separated at 300 nL/min on a gradient of 3–25% B for 90 min, 25–
864 40% B for 30 min, 40–95% B for 10 min, 95% B over 6 min, using 0.1% FA in water for A and
865 0.1% FA in 80% acetonitrile for B. The Orbitrap and FAIMSpro were operated in positive ion

866 mode with a positive ion voltage of 2100 V, an ion transfer tube temperature of 305°C, and a 4.2
867 L/min carrier gas flow, using standard FAIMS resolution and compensation voltages of -45, –55,
868 and –65 V. Full scan spectra were acquired in profile mode at a resolution of 120,000 (MS1 and
869 MS2), with a scan range of 400–1400 m/z, custom maximum fill time (200 ms), custom AGC
870 target (100% MS1, 250% MS2), isolation windows of m/z 0.7, intensity threshold of 2.0e4, 2–6
871 charge state, dynamic exclusion of 60 seconds, and 35% HCD collision energy.
872
873 *Proteomic and Phosphoproteomic Data Analysis*
874 Proteome data were analyzed using the PEAKS Studio 10.6 software package. Raw data
875 extracted from .raw files were pre-processed with the following settings: scans were merged
876 within a 10 ppm retention time window and a 10 ppm precursor m/z tolerance, including
877 precursor mass and charge states (z = 2-8). Pre-processing steps included automatic centroiding,
878 deisotoping, and deconvolution.
879 Protein identification was performed using a mouse protein FASTA database (Uniprot Taxon ID
880 10090), with the following parameters: parent mass error tolerance set to 10 ppm, fragment mass
881 error tolerance set to 0.05 Da, retention time shift tolerance of 5.0 minutes, and semispecific
882 trypsin enzyme specificity. TMT was applied as an unvariable modification, while the variable
883 modifications considered included carbamidomethylation (C), oxidation (M), phosphorylation
884 (P), and deamidation (NQ). Non-specific cleavage at one terminus was allowed, with up to three
885 missed cleavages and a maximum of three variable posttranslational modifications per peptide.
886 The false discovery rate (FDR) was estimated using the decoy-fusion approach, with peptides
887 having an FDR ≤ 1% and a significance threshold of 20 (-10lgP) considered confidently
888 identified. For protein quantification, at least two high abundant peptide signals were selected to
889 calculate raw protein peak areas. The software computed phosphosite data by using the
890 abundances of multiple peptides for each phosphorylation.

891 **References**

892 1. Perry, R. J. *et al.* Leptin Mediates a Glucose-Fatty Acid Cycle to Maintain Glucose
893 Homeostasis in Starvation. *Cell* **172**, 234-248.e17 (2018).
894 2. Geiser, F. Metabolic Rate and Body Temperature Reduction During Hibernation and Daily
895 Torpor. *Annual Review of Physiology* **66**, 239–274 (2004).
896 3. Muoio, D. M. Metabolic inflexibility: when mitochondrial indecision leads to metabolic
897 gridlock. *Cell* **159**, 1253–1262 (2014).
898 4. Lee, S.-H., Park, S.-Y. & Choi, C. S. Insulin Resistance: From Mechanisms to Therapeutic
899 Strategies. *Diabetes Metab J* **46**, 15–37 (2022).
900 5. Insulin Resistance Is Accompanied by Increased Fasting Glucagon and Delayed Glucagon
901 Suppression in Individuals With Normal and Impaired Glucose Regulation | Diabetes |
902 American Diabetes Association.
903 https://diabetesjournals.org/diabetes/article/65/11/3473/17158/Insulin-Resistance-Is-
904 Accompanied-by-Increased.
905 6. Coutinho, E. A. *et al.* Activation of SF1 Neurons in the Ventromedial Hypothalamus by
906 DREADD Technology Increases Insulin Sensitivity in Peripheral Tissues. *Diabetes* **66**,
907 2372–2386 (2017).
908 7. Flak, J. N. *et al.* Ventromedial hypothalamic nucleus neuronal subset regulates blood glucose
909 independently of insulin. *J Clin Invest* **130**, 2943–2952.
910 8. Douglass, A. M. *et al.* Neural basis for fasting activation of hypothalamic-pituitary-adrenal
911 axis. *Nature* **620**, 154–162 (2023).
912 9. Herman, J. P. *et al.* Regulation of the hypothalamic-pituitary-adrenocortical stress response.
913 *Compr Physiol* **6**, 603–621 (2016).
914 10. Ambler, M., Hitrec, T. & Pickering, A. Turn it off and on again: characteristics and control
915 of torpor. *Wellcome Open Res* **6**, 313 (2022).
916 11. Hrvatin, S., Sun, S., Wilcox, O. F., Yao, H., Lavin-Peter, A. J., Cicconet, M., Assad, E. G.,
917 Palmer, M. E., Aronson, S., Banks, A. S., Griffith, E. C., & Greenberg, M. E. (2020).
918 Neurons that regulate mouse torpor. *Nature*, *583*(7814), 115–121.
919 https://doi.org/10.1038/s41586-020-2387-5

920

921 12.Takahashi, T. M. *et al.* A discrete neuronal circuit induces a hibernation-like state in rodents.
922 *Nature* **583**, 109–114 (2020).
923 13. Yu, S. *et al.* Glutamatergic Preoptic Area Neurons That Express Leptin Receptors Drive
924 Temperature-Dependent Body Weight Homeostasis. *The Journal of Neuroscience* **36**, 5034
925 (2016).
926 14. Wang, Y. & Wu, R. The Effect of Fasting on Human Metabolism and Psychological Health.
927 *Dis Markers* **2022**, 5653739 (2022).
928 15. Roth, B. L. DREADDs for Neuroscientists. *Neuron* **89**, 683–694 (2016).
929 16. Frayn, K. N. Calculation of substrate oxidation rates in vivo from gaseous exchange. *Journal*
930 *of Applied Physiology* **55**, 628–634 (1983).
931 17. Boucher, J., Kleinridders, A. & Kahn, C. R. Insulin Receptor Signaling in Normal and
932 Insulin-Resistant States. *Cold Spring Harbor Perspectives in Biology* **6**, a009191 (2014).
933 18. Leto, D. & Saltiel, A. R. Regulation of glucose transport by insulin: traffic control of
934 GLUT4. *Nat Rev Mol Cell Biol* **13**, 383–396 (2012).
935 19. DeFronzo, R. A., Tobin, J. D. & Andres, R. Glucose clamp technique: a method for
936 quantifying insulin secretion and resistance. *Am J Physiol* **237**, E214-223 (1979).
937 20. Kim, J. K. Hyperinsulinemic–Euglycemic Clamp to Assess Insulin Sensitivity In Vivo. in
938 *Type 2 Diabetes: Methods and Protocols* (ed. Stocker, C.) 221–238 (Humana Press, Totowa,
939 NJ, 2009). doi:10.1007/978-1-59745-448-3_15.
940 21. DeFronzo, R. A. & Tripathy, D. Skeletal Muscle Insulin Resistance Is the Primary Defect in
941 Type 2 Diabetes. *Diabetes Care* **32**, S157–S163 (2009).
942 22. Rudolf, R., Kettelhut, I. C. & Navegantes, L. C. C. Sympathetic innervation in skeletal
943 muscle and its role at the neuromuscular junction. *J Muscle Res Cell Motil* **45**, 79–86 (2024).
944 23. Kalinovich, A. *et al.* Treatment with a β-2-adrenoceptor agonist stimulates glucose uptake in
945 skeletal muscle and improves glucose homeostasis, insulin resistance and hepatic steatosis in
946 mice with diet-induced obesity. *Diabetologia* **63**, 1603–1615 (2020).
947 24. Navegantes, L. C., Resano, N. M., Migliorini, R. H. & Kettelhut, I. C. Effect of
948 guanethidine-induced adrenergic blockade on the different proteolytic systems in rat skeletal
949 muscle. *Am J Physiol* **277**, E883-889 (1999).
950 25. Megeney, L. A. *et al.* Regulation of muscle glucose transport and GLUT-4 by nerve-derived
951 factors and activity-related processes. *Am J Physiol* **269**, R1148-1153 (1995).

952 26. Marinelli, M., Rougé-Pont, F., De Jesus-Oliveira, C., Le Moal, M. & Piazza, P. V. Acute
953 blockade of corticosterone secretion decreases the psychomotor stimulant effects of cocaine.
954 *Neuropsychopharmacology* **16**, 156–161 (1997).
955 27. Yang, H. *et al.* A novel H129-based anterograde monosynaptic tracer exhibits features of
956 strong labeling intensity, high tracing efficiency, and reduced retrograde labeling. *Mol*
957 *Neurodegener* **17**, 6 (2022).
958 28. Kataoka, N., Hioki, H., Kaneko, T. & Nakamura, K. Psychological Stress Activates a
959 Dorsomedial Hypothalamus-Medullary Raphe Circuit Driving Brown Adipose Tissue
960 Thermogenesis and Hyperthermia. *Cell Metabolism* **20**, 346–358 (2014).
961 29. Madden, C. J. & Morrison, S. F. Excitatory amino acid receptor activation in the raphe
962 pallidus area mediates prostaglandin-evoked thermogenesis. *Neuroscience* **122**, 5–15 (2003).
963 30. Moffitt, J. R. *et al.* Molecular, spatial, and functional single-cell profiling of the
964 hypothalamic preoptic region. *Science* **362**, eaau5324 (2018).
965 31. Tan, C. L. *et al.* Warm-Sensitive Neurons that Control Body Temperature. *Cell* **167**, 47-
966 59.e15 (2016).
967 32. Roh, E., Song, D. K. & Kim, M.-S. Emerging role of the brain in the homeostatic regulation
968 of energy and glucose metabolism. *Exp Mol Med* **48**, e216–e216 (2016).
969 33. Lee, ML., Chang, CP., Toda, C. *et al.* Body temperature regulates glucose metabolism and
970 torpid behavior. *Nat Commun* **16**, 6278 (2025). https://doi.org/10.1038/s41467-025-61499-2
971 34. Rubio, W. B., Cortopassi, M. D., Ramachandran, D., Walker, S. J., Balough, E. M., Wang, J.,
972 & Banks, A. S. (2023). Not so fast: Paradoxically increased variability in the glucose
973 tolerance test due to food withdrawal in continuous glucose-monitored mice. *Molecular*
974 *metabolism*, *77*, 101795. https://doi.org/10.1016/j.molmet.2023.101795
975 35. Deem, J. D. *et al.* Warm Responsive Neurons in the Hypothalamic Preoptic Area are Potent
976 Regulators of Glucose Homeostasis in Male Mice. *Endocrinology* **164**, bqad074 (2023).
977 36. Allen, W. E. *et al.* Thirst-associated preoptic neurons encode an aversive motivational drive.
978 *Science* **357**, 1149–1155 (2017).
979 37. Dagogo-Jack, S. Leptin and Insulin Sensitivity: Endogenous Signals of Metabolic
980 Homeostasis. *The Journal of Clinical Endocrinology & Metabolism* **109**, e1402–e1403
981 (2024).

982 38. Shimogori, T., Abe, A., Go, Y., Hashikawa, T., Kishi, N., Kikuchi, S. S., Kita, Y., Niimi, K.,
983 Nishibe, H., Okuno, M., Saga, K., Sakurai, M., Sato, M., Serizawa, T., Suzuki, S.,
984 Takahashi, E., Tanaka, M., Tatsumoto, S., Toki, M., U, M., … Okano, H. (2018). Digital
985 gene atlas of neonate common marmoset brain. *Neuroscience research*, *128*, 1–13.
986 https://doi.org/10.1016/j.neures.2017.10.009
987 39. Kita, Y., Nishibe, H., Wang, Y., Hashikawa, T., Kikuchi, S. S., U, M., Yoshida, A. C.,
988 Yoshida, C., Kawase, T., Ishii, S., Skibbe, H., & Shimogori, T. (2021). Cellular-resolution
989 gene expression profiling in the neonatal marmoset brain reveals dynamic species- and
990 region-specific differences. *Proceedings of the National Academy of Sciences of the United*
991 *States of America*, *118*(18), e2020125118. https://doi.org/10.1073/pnas.2020125118
992 40. Weir J. B. (1949). New methods for calculating metabolic rate with special reference to
993 protein metabolism. *The Journal of physiology*, *109*(1-2), 1–9.
994 https://doi.org/10.1113/jphysiol.1949.sp004363
995 41. Møller, L. L. V., Raun, S. H., Fritzen, A. M., & Sylow, L. (2022). Measurement of skeletal
996 muscle glucose uptake in mice in response to acute treadmill running. *Journal of biological*
997 *methods*, *9*(3), e162. https://doi.org/10.14440/jbm.2022.385
998 42. Volodin, A., Kosti, I., Goldberg, A. L., & Cohen, S. (2017). Myofibril breakdown during
999 atrophy is a delayed response requiring the transcription factor PAX4 and desmin
1000 depolymerization. *Proceedings of the National Academy of Sciences of the United States of*
1001 *America*, *114*(8), E1375–E1384. https://doi.org/10.1073/pnas.1612988114
1002 43. Hughes, C. S., Moggridge, S., Müller, T., Sorensen, P. H., Morin, G. B., & Krijgsveld, J.
1003 (2019). Single-pot, solid-phase-enhanced sample preparation for proteomics
1004 experiments. *Nature protocols*, *14*(1), 68–85. https://doi.org/10.1038/s41596-018-0082-x

1005 **Acknowledgements:** We thank T. Diefenbach for his help with whole brain imaging
1006 experiments. We thank all Hrvatin Lab members for their insightful comments on the
1007 manuscript. Whole brain imaging was performed at the Ragon Institute Microscopy Core.
1008 Metabolomics experiments were performed with the Whitehead Institute Metabolomics Core.
1009 Proteomic and phosphoproteomics experiments were performed with the Whitehead Institute
1010 Quantitative Proteomics Core. Metabolic cage experiments were performed at the BIDMC
1011 Energy Balance Core. Metabolic clamp experiments were performed at the UMass Metabolic
1012 Disease Research Center.
1013
1014 **Funding:**
1015 Mathers Foundation Grant (S.H.)
1016 Searle Scholars Program (S.H.)
1017 Pew Charitable Trust (S.H.)
1018 Rosenkranz Foundation (S.H.)
1019 MIT Research Support Committee Grant (S.H.)
1020 Howard Hughes Medical Institute Hrabowski Scholar (S.H.)
1021 NIH Director New Innovator Award DP2 DP2DK136123 (S.H.)
1022
1023 **Author Contributions:**
1024 J.M.R and S.H conceptualized the project. J.M.R, S.H., E.C.G, J.K.K, F.S, and A.S.B devised
1025 experimental methodologies. J.M.R, M.A, N.N, H.W, M.M, M.W, B.L, B-Y.K, and B.K
1026 executed experiments. J.M.R, S.H, M.A, N.N, and H.W contributed to data visualization. S.H
1027 and E.C.G acquired funding. S.H and E.C.G administered and supervised the project. J.M.R,
1028 S.H, and E.C.G wrote the initial manuscript draft. J.M.R, S.H, E.C.G, M.A, N.N, H.W, A.S.B,
1029 and J.K.K reviewed and edited the manuscript.
1030
1031 **Competing Interests:**
1032 The authors declare they have no competing interests
1033
1034 **Data and Material Availability:**

All data needed to evaluate conclusions made in both main text and supplementary figures in this paper will be made available upon reasonable request.

Supplementary Materials

Materials and Methods

Figs S1 to S7

Figures

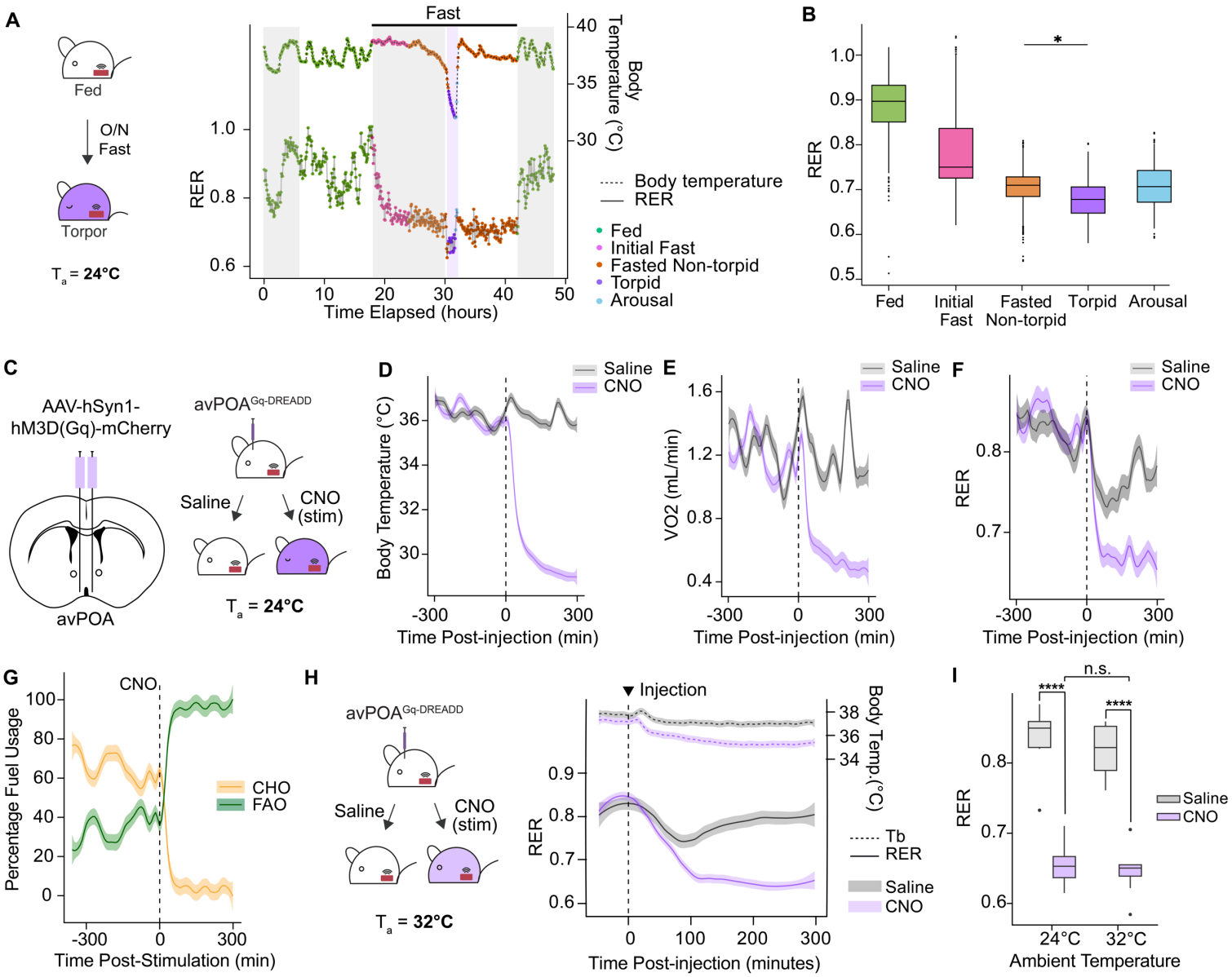

1040 **Figure 1: avPOA^{Vglut2} neurons regulate fuel usage in natural and induced torpor. (A)** *(Left)*
1041 Schematic for respirometry experiments involving natural torpor. Probe-implanted wild-type
1042 C57Bl6/J mice were monitored throughout a 24-hour fast (ZT12-ZT12, denoted by horizontal
1043 line). (*Right)* Representative traces of respiratory exchange ratio (RER, bottom, solid line) and

1044 body temperature (T_b, top, dashed line) for an animal undergoing natural fasting-induced torpor.
1045 Traces were classified into distinct states based on food availability and T_b: *Fed*, ad libitum
1046 access to chow; *Initial Fast*, <6 h post-food withdrawal; *Fasted Non-torpid*, >6 h fasting and T_b >
1047 34.5°C; Torpid –fasted, T_b < 34.5°C, and ΔT_b < 0; *Arousal*, T_b < 35.5°C and ΔT_b > 0. Shaded
1048 gray portions denote dark cycle times (ZT12-24). **(B)** State-dependent quantification of RER for
1049 fasted mice as in (A) (n = 8 animals, 4 male, 4 female, * = $p < 0.05$). **(C)** (*Left)* Schematic for
1050 bilateral stereotactic transduction of avPOA neurons with Gq-DREADD. ***(Right)*** Experimental
1051 paradigm for stimulating avPOA-transduced animals with either saline or CNO (1 mg/kg) at T_a =
1052 24°C. (**D-F)** Quantification of T_b (**D**), VO_2 (**E**), and RER (**F**) in Gq-DREADD-expressing mice
1053 for 300 minutes pre- and post-CNO stimulation (dashed vertical line). Traces and shading
1054 indicate mean ± SEM (n = 8 animals). **(G)** Calculation of carbohydrate oxidation (CHO) and
1055 fatty acid oxidation (FAO) percentages for 300 minutes pre- and post-CNO injection (dashed
1056 vertical line) based on the method of Frayn (see Methods). **(H)** (*Left*) Following acclimation at
1057 elevated T_a (32°C), Gq-DREADD-expressing mice were administered either saline or CNO and
1058 monitored for gas exchange and T_b. (*Right)* RER and T_b changes in Gq-DREADD-expressing
1059 mice in response to CNO stimulation or saline control. Dashed vertical line indicates timing of
1060 the injection. Ambient temperature denoted by horizontal dashed line (T_a = 32°C). **(I)**
1061 Quantitation of RER 300 min following CNO or saline control injections at T_a = 24°C or 32°C
1062 (**** = $p < 0.00005$, n = 8 mice).

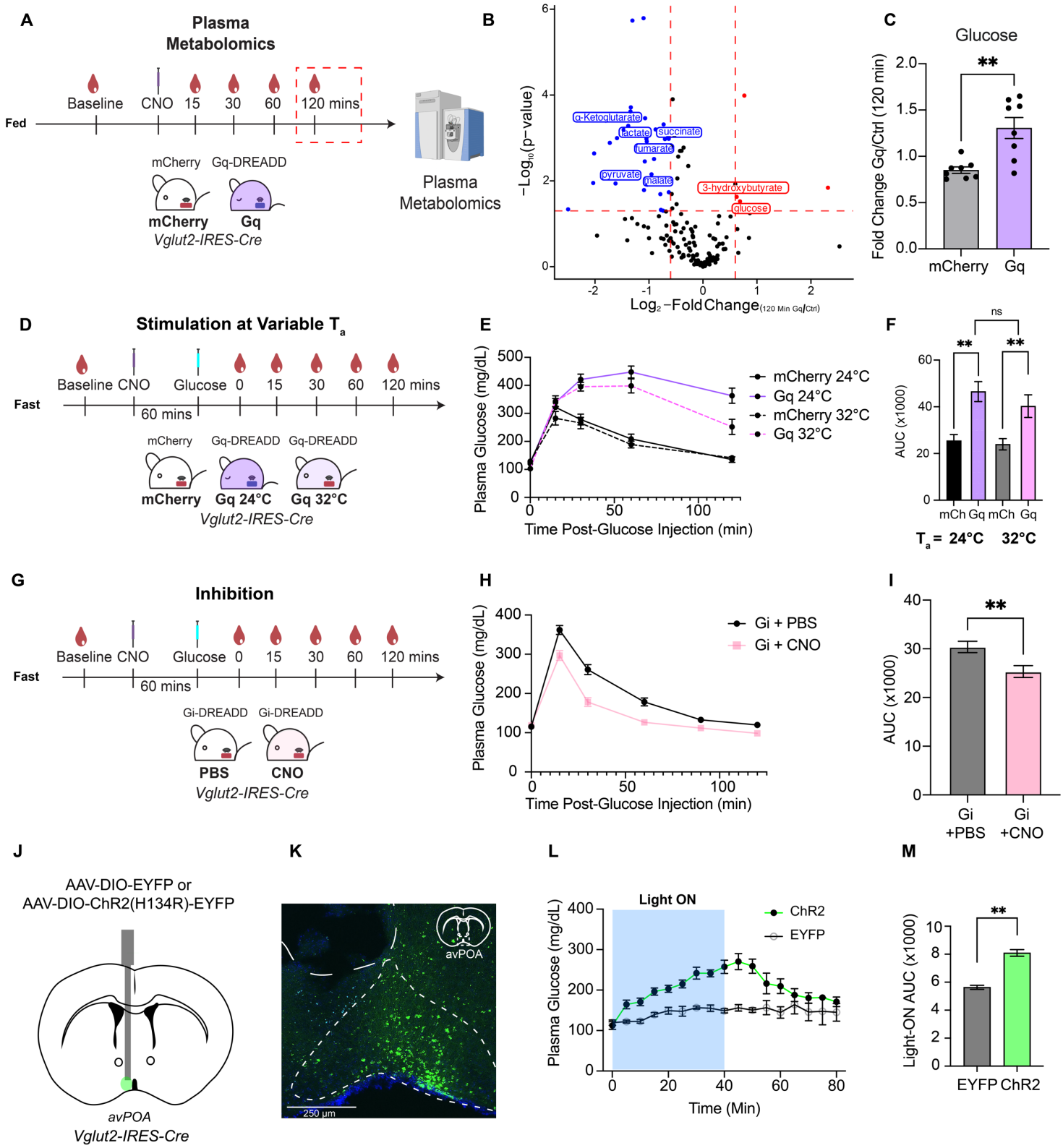

Figure 2: avPOA^{Vglut2} neuronal regulation of whole-body glucose homeostasis is rapid and reversible. (A) Schematic of blood sampling protocol for plasma metabolomics from mCherry-

1065 and Gq-DREADD-transduced *Vglut2-IRES-Cre* mice pre- and post-CNO administration. n = 8
1066 mice (4 female, 4 male) per cohort. Blood samples were taken 0, 15, 30, 60, and 120 min post-
1067 CNO injection (1 mg/kg) for plasma separation, LC/MS, and polar metabolomics analysis. **(B)**
1068 (*Left*) Volcano plot of differentially altered metabolites 120 min post-CNO administration.
1069 Selected overrepresented and underrepresented metabolites labeled in red and blue, respectively.
1070 p-values calculated using two-tailed t-test, red lines corresponding to FDR-corrected $p < 0.05$,
1071 and $|Log_2\text{-Fold change}| > 0.6$. **(C)** Fold-change in glucose abundance in Gq-DREADD-
1072 expressing vs. mCherry control mice at 120 min post-CNO injection. (n = 8 animals, mean
1073 ±SEM, ** = $p<0.005$, two-tailed t-test). **(D)** Schematic for intraperitoneal glucose tolerance test
1074 (GTT) in Gq-DREADD and mCherry control mice. Animals were fasted for 3h prior to baseline
1075 glucose measurement and CNO administration. Subsequent to a 60-minute interval following
1076 CNO administration, a baseline blood sample was taken, animals were injected with glucose (2
1077 g/kg), and subsequent blood samples for changes in glucose levels were obtained at 15, 30, 60,
1078 and 120 min post glucose administration. **(E)** Glucose tolerance testing of mCherry (Ctrl) or Gq-
1079 DREADD-expressing animals at T_a = 24°C or 32°C (24°C: n = 13 mCherry, n = 14 Gq; 32°C: n
1080 = 14 mCherry, n=16 Gq *Vglut2-IRES-Cre* animals, mean ±SEM). **(F)** Area under the curve
1081 (AUC) quantification of (E) in all cohorts (** = $p < 0.005$, student's two-tailed t-test, mean
1082 ±SEM). **(G)** Schematic for GTT in Gi-DREADD-transduced *Vglut2-IRES-Cre* animals. Gi-
1083 DREADD-expressing animals were injected with either PBS or CNO (10 mg/kg) prior to GTT,
1084 and blood was collected as in other GTT experiments. **(H)** Glucose tolerance testing of PBS- and
1085 CNO-injected Gi-DREADD animals (n = 8 PBS, n = 8 CNO, mean ±SEM). **(I)** AUC
1086 quantification of GTT in (H) for PBS- and CNO-injected experiments (** = $p < 0.005$, student's
1087 paired two-tailed t-test, mean ±SEM). **(J)** Schematic of unilateral stereotactic administration of
1088 AAV-DIO-ChR2(H134R)-EYFP or AAV-DIO-EYFP to the avPOA of *Vglut2-IRES-Cre* mice
1089 (n=4 EYFP, n= 5 ChR2). **(K)** Representative image of (J), showing ChR2-EYFP signal in an
1090 experimental animal (Scale bar = 250 μm). **(L)** Plasma glucose sampling of ChR2- and EYFP-
1091 expressing mice for 80 min at 5 min intervals (Light ON 0-40 minutes, indicated by blue
1092 shading; Light OFF 41-80 minutes, indicated by no shading, mean ±SEM). **(M)** AUC
1093 quantification of (L) (** = $p < 0.005$, Students two-tailed t-test, n = 4 EYFP, n = 5 ChR2 *Vglut2-*
1094 *IRES-Cre* animals).

1095

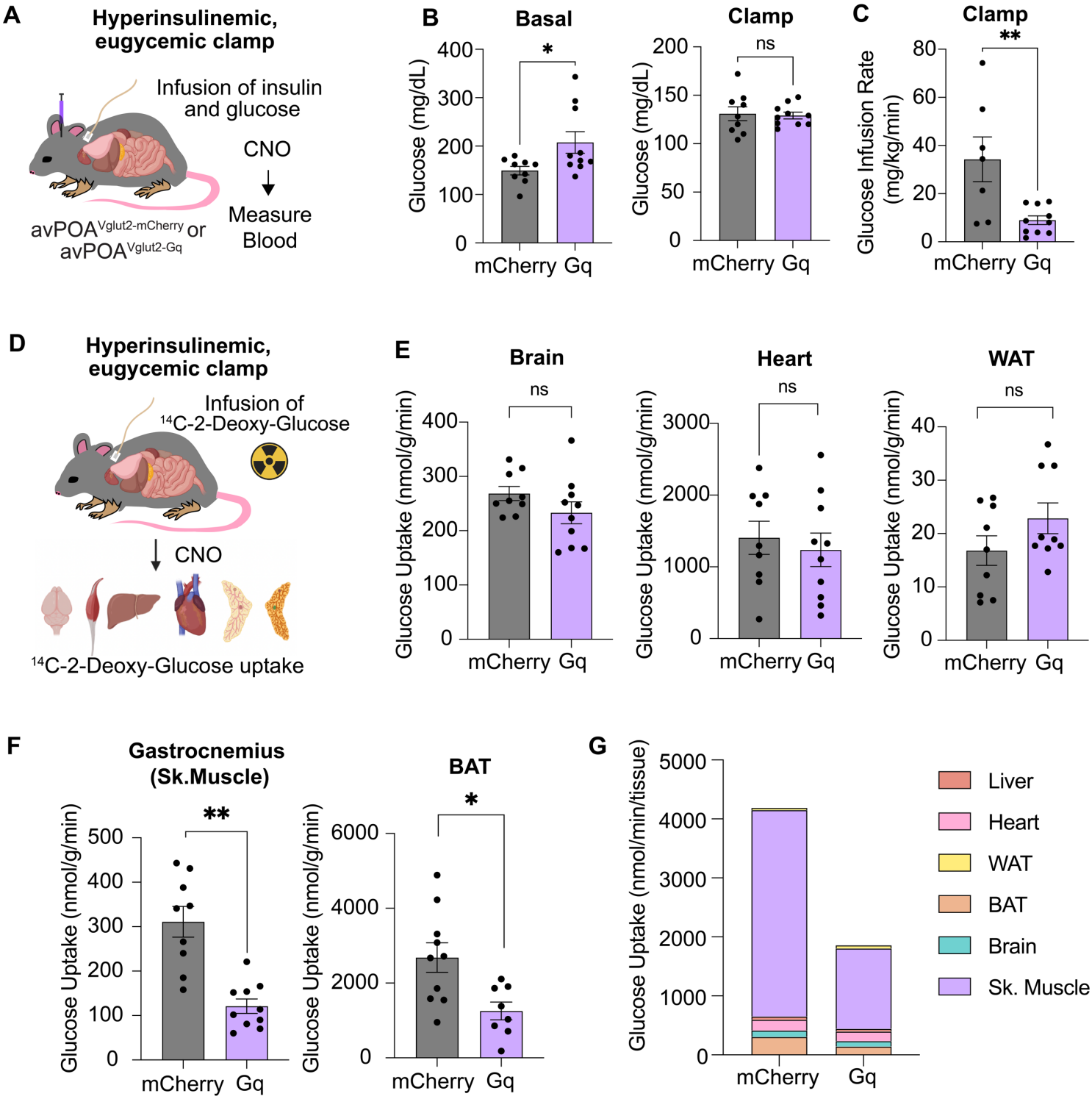
A
Hyperinsulinemic, eugycemic clamp
Infusion of insulin and glucose
CNO
Measure Blood
avPOA Vglut2-mCherry or avPOA Vglut2-Gq
B
Basal
Glucose (mg/dL)
400
300
200
100
0
*
mCherry Gq
Clamp
Glucose (mg/dL)
200
150
100
50
0
ns
mCherry Gq
C
Clamp
Glucose Infusion Rate (mg/kg/min)
80
60
40
20
0
**
mCherry Gq
D
Hyperinsulinemic, eugycemic clamp
Infusion of 14C-2-Deoxy-Glucose
CNO
14C-2-Deoxy-Glucose uptake
E
Brain
Glucose Uptake (nmol/g/min)
400
300
200
100
0
ns
mCherry Gq
Heart
Glucose Uptake (nmol/g/min)
3000
2000
1000
0
ns
mCherry Gq
WAT
Glucose Uptake (nmol/g/min)
40
30
20
10
0
ns
mCherry Gq
F
Gastrocnemius (Sk.Muscle)
Glucose Uptake (nmol/g/min)
500
400
300
200
100
0
**
mCherry Gq
BAT
Glucose Uptake (nmol/g/min)
6000
4000
2000
0
*
mCherry Gq
G
Glucose Uptake (nmol/min/tissue)
5000
4000
3000
2000
1000
0
mCherry
Gq
Liver
Heart
WAT
BAT
Brain
Sk. Muscle

1096 **Figure 3: avPOA ^{Vglut2} neurons coordinate whole-body glucose hypometabolism and organ-**
1097 **specific defects in glucose uptake. (A)** Schematic for hyperinsulinemic-euglycemic clamp and
1098 tissue-specific glucose uptake measurements. Gq-DREADD- or mCherry-transduced animals
1099 were implanted with indwelling catheters, mildly restrained, and subjected to continuous
1100 infusion of glucose, insulin, ^{3}H-glucose, and ^{14}C-2-deoxyglucose over the course of the two-hour
1101 experiment. Glucose levels were maintained at approximately 120 mg/dL to ensure clamp
1102 effectiveness. Animals were sacrificed, and the displayed tissues were taken for radioactive ^{14}C-
1103 2-Deoxyglucose-6-Phosphate uptake analysis. **(B)** Glucose levels 60 min after CNO stimulation
1104 (Basal) were significantly elevated in Gq-DREADD-expressing animals as compared to control
1105 animals (* = $p<0.05$, student's two-tailed t-test, mCherry = 149.4 ± 8.8 mg/dL; Gq = 207.5 ±
1106 22.2 mg/dL, mean ±SEM, n= 9 mCherry, n=10 Gq *Vglut2-IRES-Cre* animals). Conversely,
1107 during the hyperinsulinemic clamp, Gq-DREADD- and mCherry-expressing animals maintained
1108 nearly identical levels plasma glucose (Gq: 130.9 ± 7.2 mg/dL, mCherry: 129.1 ± 3.4 mg/dL),
1109 indicating successful clamping of plasma glucose. **(C)** Glucose Infusion Rate (GIR) of control
1110 (mCherry) and Gq-DREADD-transduced animals throughout the 120-minute duration of the
1111 experiment (** = $p < 0.005$, student's two-tailed t-test, mean ±SEM). **(D)** Organs in which
1112 avPOA stimulation had no significant effect on insulin-stimulated glucose uptake (ns = $p > 0.05$,
1113 student's two-tailed t-test, mean ±SEM). **(E)** Gastrocnemius and BAT exhibited reductions of
1114 61.1% and 55.3% in ^{14}C-2-DG-6-Phosphate uptake (Glucose Uptake), respectively, between Gq-
1115 DREADD- and mCherry-expressing animals (* = $p < 0.05$, ** = $p< 0.005$, student's two-tailed t-
1116 test, mean ±SEM). **(F)** Calculated mass-dependent glucose uptake in each of the six examined
1117 organs based on average tissue weights of control and Gq-DREADD-expressing animals and
1118 tissue-specific glucose uptake rates (Mass-Dependent Uptake (nmol/min) = Average Tissue
1119 Mass (g) * Glucose Uptake Rate (nmol/min/g tissue)).

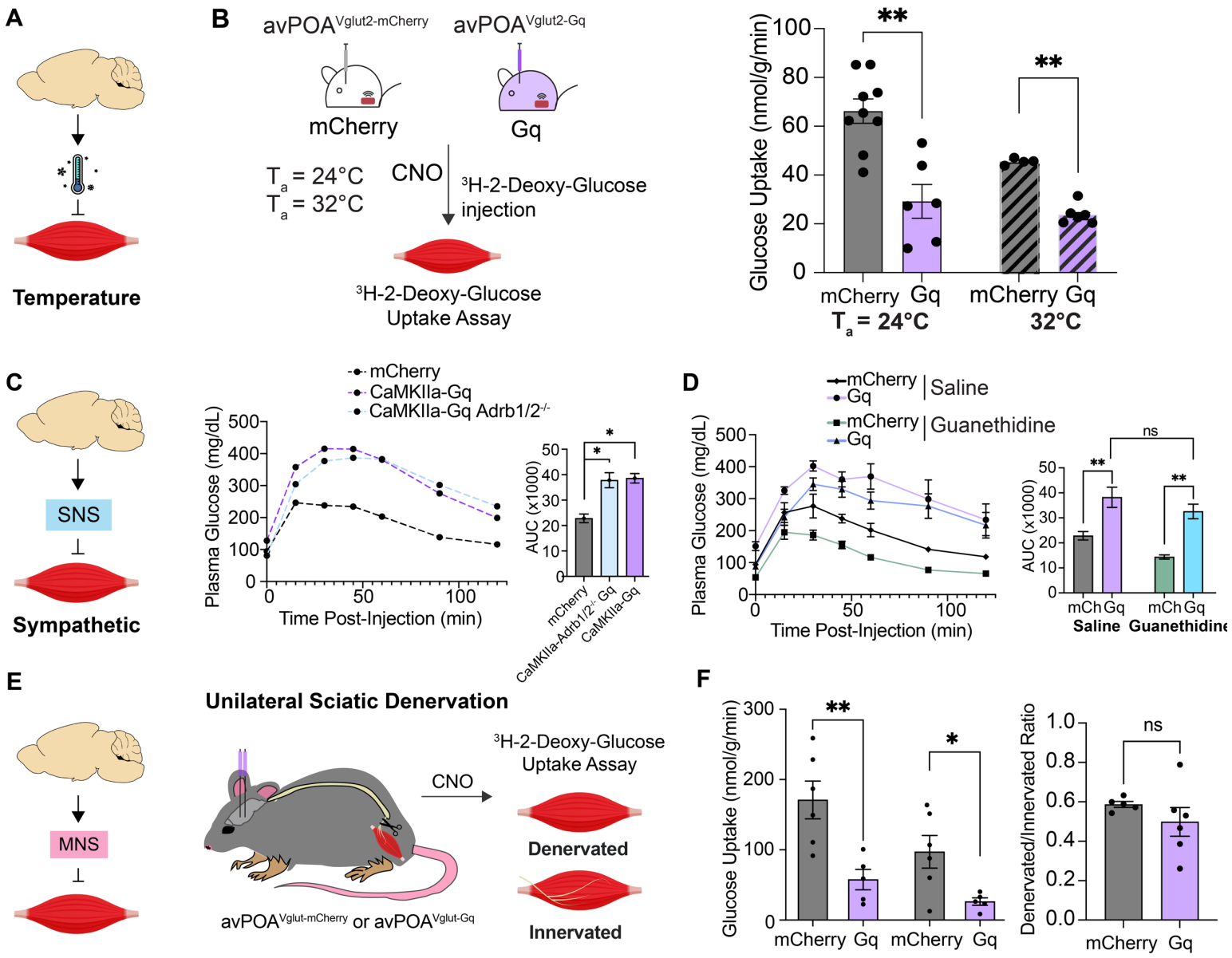
A
Temperature
B
avPOA Vglut2-mCherry
avPOA Vglut2-Gq
mCherry
Gq
Ta = 24°C
Ta = 32°C
CNO
3H-2-Deoxy-Glucose injection
3H-2-Deoxy-Glucose Uptake Assay
Glucose Uptake (nmol/g/min)
mCherry Gq
Ta = 24°C
mCherry Gq
32°C
C
SNS
Sympathetic
mCherry
CaMKIIa-Gq
CaMKIIa-Gq Adrb1/2-/-
Plasma Glucose (mg/dL)
Time Post-Injection (min)
AUC (x1000)
mCherry
CaMKIIa-Adrb1/2-/- Gq
CaMKIIa-Gq
D
mCherry
Gq
Saline
mCherry
Gq
Guanethidine
Plasma Glucose (mg/dL)
Time Post-Injection (min)
AUC (x1000)
ns
mCh Gq
Saline
mCh Gq
Guanethidine
E
MNS
Unilateral Sciatic Denervation
CNO
3H-2-Deoxy-Glucose Uptake Assay
Denervated
Innervated
avPOA Vglut-mCherry or avPOA Vglut-Gq
F
Glucose Uptake (nmol/g/min)
mCherry Gq
mCherry Gq
Denervated/Innervated Ratio
ns
mCherry Gq

1120 **Figure 4: Determination of peripheral effectors of avPOA^{Vglut2}-induced skeletal muscle**
1121 **insulin resistance. (A)** Schematic for potential temperature-regulated effects of avPOA^{Vglut2}
1122 neuronal stimulation on skeletal muscle glucose uptake. **(B)** (*Left*) Schematic for radioactive
1123 glucose (^{3}H-2-deoxyglucose-6 phosphate) uptake assay in *Vglut2-IRES-Cre* animals injected
1124 with either Cre-dependent mCherry (avPOA$^{Vglut2\text{-}mCherry}$) or Gq-DREADD (avPOA$^{Vglut2\text{-}Gq}$), then
1125 pretreated with CNO and subjected to radioactive glucose uptake assay at T_a = 24°C or 32°C.
1126 (*Right)* results of Radioactive glucose (^{3}H-2-deoxyglucose-6 phosphate) uptake assay in
1127 gastrocnemius muscles of control (avPOA$^{Vglut2\text{-}mCherry}$) or Gq-DREADD (avPOA$^{Vglut2\text{-}Gq}$) mice
1128 housed at T_a =24°C or 32°C (** = $p < 0.005$, student's two-tailed t-test, mean ±SEM, n = 9
1129 mCherry 24°C , n = 6 Gq 24°C, n = 4 mCherry 32°C, n=6 Gq 32°C *Vglut2-IRES-Cre* animals).
1130 **(C)** Glucose tolerance testing of control mCherry-expressing mice (mCherry), mice transduced
1131 with AAV-CaMKIIa-hM3D(Gq)-mCherry (CaMKIIa-Gq), and CaMKIIa-Gq-transduced
1132 *Adrb1/2$^{-/-}$* mice (CaMKIIa-Gq Adrb1/2$^{-/-}$). AUC calculation shown on right (* = $p < 0.05$,
1133 student's two-tailed t-test, mean ±SEM, n = 6 Vglut-mCherry, n = 6 CaMKIIa-Gq, n = 4
1134 CaMKIIa-Gq Adrb1/2$^{-/-}$ animals). **(D)** Pair-matched glucose tolerance tests in animals injected
1135 with saline, CNO (1 mg/kg), Guanethidine (50 mg/kg), or Guanethidine and CNO (ns = $p > 0.05$,
1136 ** = $p < 0.005$, paired student's two-tailed t-test, mean ±SEM, n = 6 mice per condition). **(E)**
1137 Schematic of sciatic nerve denervation paradigm to test the requirement for motor innervation
1138 for avPOA-induced skeletal muscle insulin resistance. Unilateral denervation allows for a
1139 matched innervated internal control. **(F)** Radioactive glucose uptake assay in innervated or
1140 denervated gastrocnemius muscle in CNO-treated control mCherry- and Gq-DREADD-
1141 expressing animals (mCherry innervated = 171.0±26.9, Gq innervated = 57.6±14.5, mCherry
1142 denervated = 97.1±23.2, Gq denervated = 26.3±5.3 nmol/g/min). (*Right*) Ratio of
1143 denervated:innervated gastrocnemius glucose uptake in mCherry animals (59.9±1.5%) and Gq
1144 animals (49.0±7.3%).

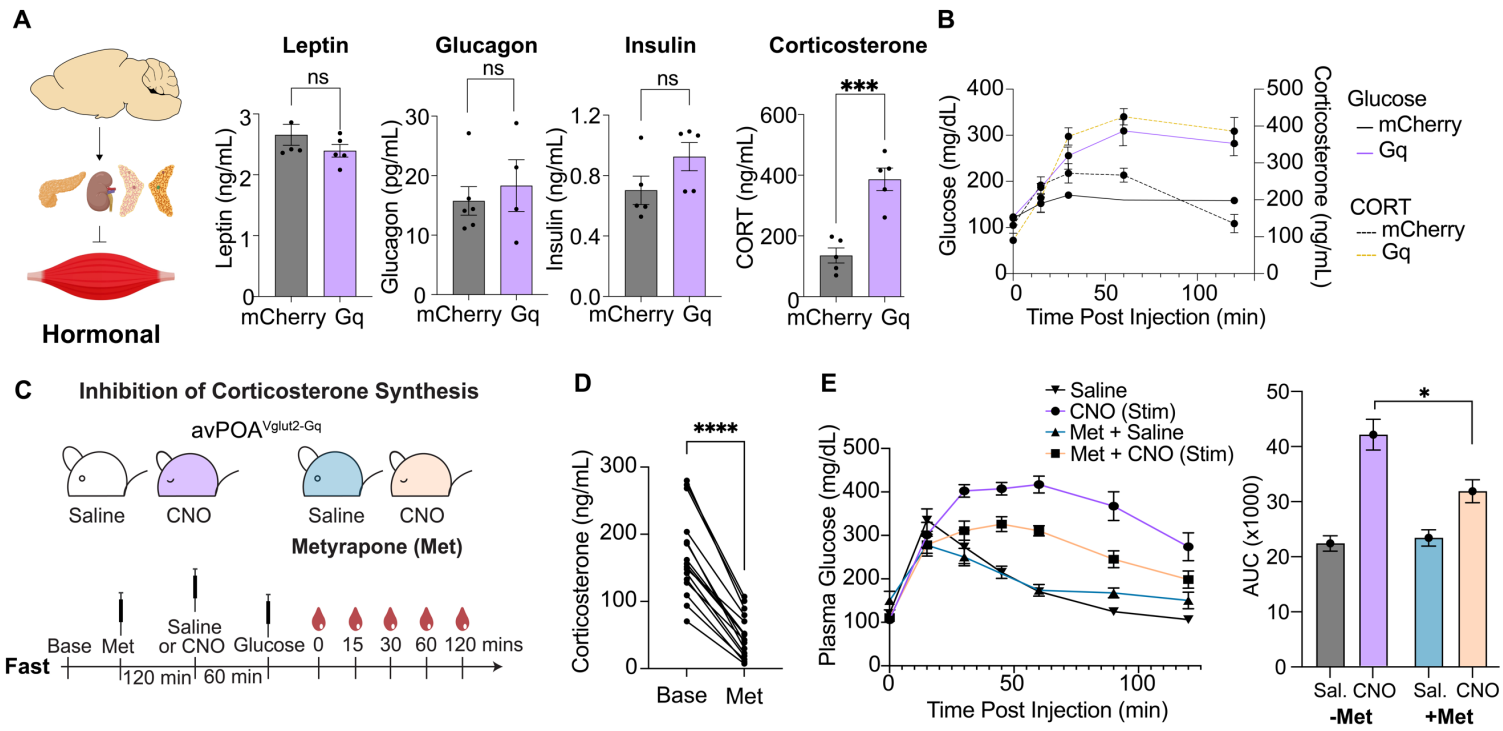

Figure 5: avPOA-induced insulin intolerance requires corticosterone. (A) Concentrations of plasma leptin, glucagon, insulin, and corticosterone 60 minutes following CNO administration in fed mCherry- and Gq-DREADD-expressing animals. (Leptin: n = 5 mCherry, n = 5 Gq; Glucagon: n= 5 mCherry, n = 6 Gq; Insulin: n = 5 mCherry, n = 5 Gq; Corticosterone: n = 5 mCherry, n = 7 Gq animals, ** = $p < 0.005$). **(B)** Longitudinal monitoring of glucose and corticosterone in fed mCherry- and Gq-expressing mice injected with 1 mg/kg CNO. Blood plasma taken 0, 15, 30, 60, and 120 minutes post-injection (n = 7 Gq, n = 5 mCherry Vglut2-IRES-Cre animals). **(C)** Schematic for metyrapone treatment during glucose tolerance testing. Animals were fasted for 120 minutes before baseline blood glucose levels were taken. Animals were then injected with 50 mg/kg metyrapone, and CNO was administered 2 hours following metyrapone injection. Subsequently, the GTT proceeded as previously described. **(D)** Corticosterone ELISA on blood sampled from animals prior to metyrapone injection (Base) or 2 hours post-injection (Met) (**** = $p<0.00005$, student's two-tailed t-test, mean ±SEM, n = 6 samples per condition). **(E)** Glucose tolerance test of Gq-DREADD-transduced *Vglut2-IRES-Cre* animals injected with saline, CNO (1 mg/kg), saline + metyrapone (50 mg/kg), or CNO (1 mg/kg) + metyrapone (50 mg/kg). (*Right*) AUC quantitation of results (* = $p < 0.05$, student's two=tailed t-test, mean ±SEM, n = 6 *Vglut2-IRES-Cre* animals).

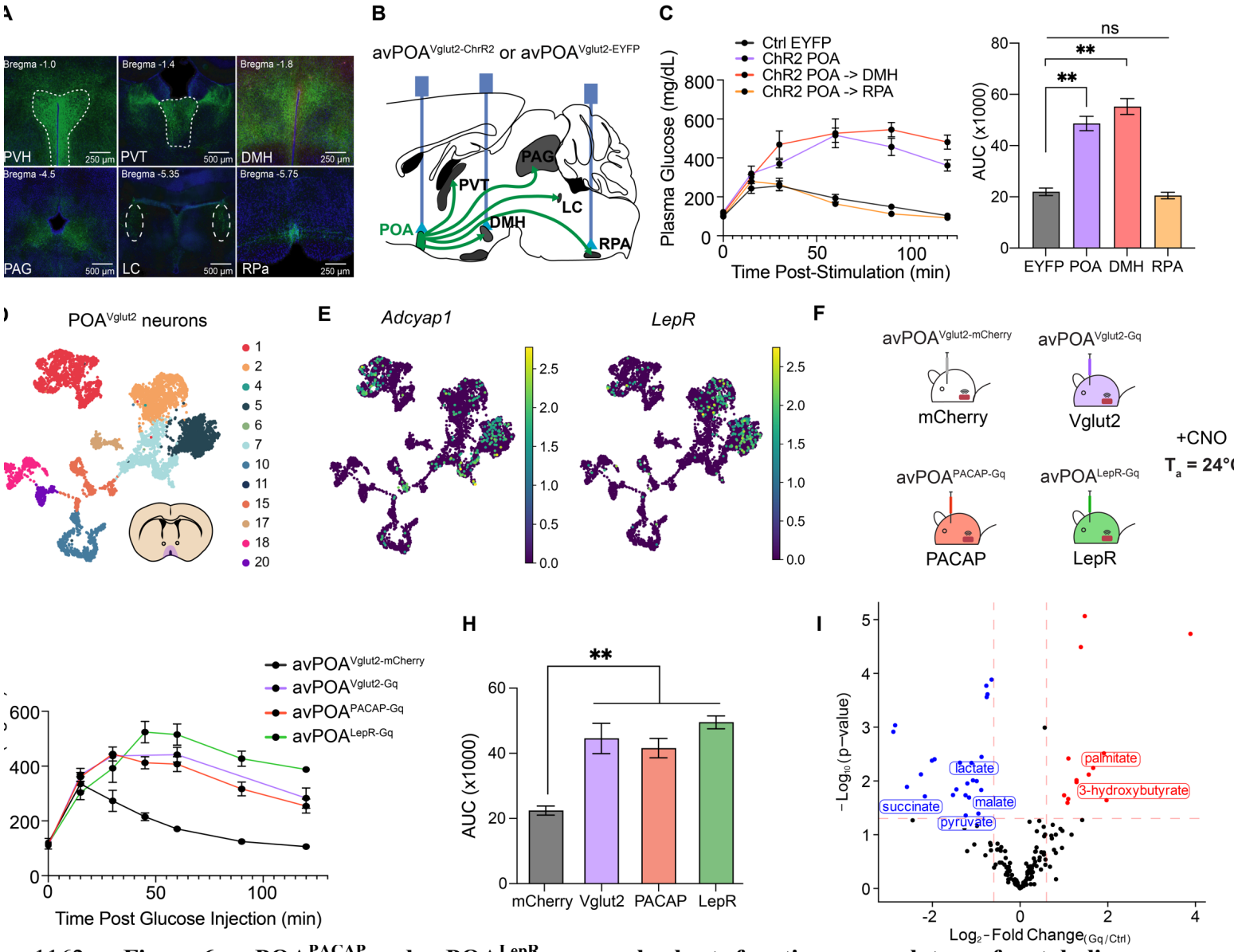

Figure 6: avPOA^{PACAP} and avPOA^{LepR} neuronal subsets function as regulators of metabolic flexibility. (A) Immunostaining of axonal fibers in *Vglut2-IRES-Cre* mice transduced with Gq-DREADD (AAV-hSyn-DIO-hM3D(Gq)-mCherry). Axonal projections were identified in a variety of downstream regions, including the paraventricular thalamus (PVT), paraventricular hypothalamus (PVH), dorsomedial hypothalamus (DMH), periacqueductal grey (PAG), locus coeruleus (LC), and raphe pallidus (RPa). **(B)** Optogenetic branch stimulation of hindbrain-projecting avPOA^{Vglut2} neurons. Blue bars correspond to regions targeted for optogenetic stimulation via cannula implantation and subsequent exposure to 455 nm blue light. **(C)** (*Left)* Glucose tolerance testing of *Vglut2-IRES-Cre* animals transduced with a Cre-dependent ChR2 (AAV-DIO-ChR2(H134R)-EYFP) or EYFP (AAV-DIO-EYFP) with optic fibers placed

1172 unilaterally above either the POA, POA→DMH-projecting neurons, or POA→RPA-projecting
1173 neurons. *(Right)* AUC of GTT for each cohort described (ns = $p > 0.05$, ** = $p < 0.005$, student's
1174 two-tailed t-test, mean ±SEM, n = 4 EYFP, n = 4 POA, n = 3 POA→DMH, n = 3 POA→RPa
1175 *Vglut2-IRES-Cre* animals). **(D)** UMAP plot and Leiden clustering of all avPOA^{Vglut2} neurons
1176 identified in Hrvatin et al., 2020. **(E)** UMAP plot of avPOA^{Vglut2} neurons colored by *Adcyap1*
1177 and *LepR* expression. **(F)** Schematic showing four groups of animals: mCherry (mCherry-
1178 transduced *Vglut2-IRES-Cre,* n = 11), Vglut2 (Gq-DREADD transduced *Vglut2-IRES-Cre*)
1179 (n=10), PACAP (Gq-DREADD-transduced *PACAP-2A-Cre*) (n=11), and LepR (Gq-DREADD-
1180 transduced *LepR-IRES-Cre* (n=3) animals injected with 1 mg/kg CNO. **(G)** Glucose tolerance
1181 test of mCherry (avPOA$^{Vglut2\text{-}mCherry}$), Vglut2 (avPOA$^{Vglut2\text{-}Gq}$), PACAP (avPOA$^{PACAP\text{-}Gq}$), and
1182 LepR (avPOA$^{LepR\text{-}Gq}$), animals from (F). **(H)** AUC analysis for (G) (** = $p < 0.05$, student's two-
1183 tailed t-test, mean ±SEM, n=7 avPOA$^{Vglut2\text{-}mCherry}$, n = 10 avPOA$^{Vglut2\text{-}Gq}$, n = 11 avPOA$^{PACAP\text{-}Gq}$,
1184 n = 3 avPOA$^{LepR\text{-}Gq}$ animals). (**I**) Volcano Plot of 120-minute polar metabolomics of *PACAP-2A-*
1185 *Cre* animals transduced with a Cre-dependent Gq-DREADD and injected with either PBS or
1186 CNO (1 mg/kg). Animals were treated as in **Figures 2a-c**. Selected overrepresented and
1187 underrepresented metabolites labeled in red and blue, respectively. p-values calculated using
1188 two-tailed t-test; red lines corresponding to p-value and Log_2-Fold changes set at $p < 0.05$ and
1189 $|Log_2\text{-Fold change}| > 0.6$.

Supplementary Figures

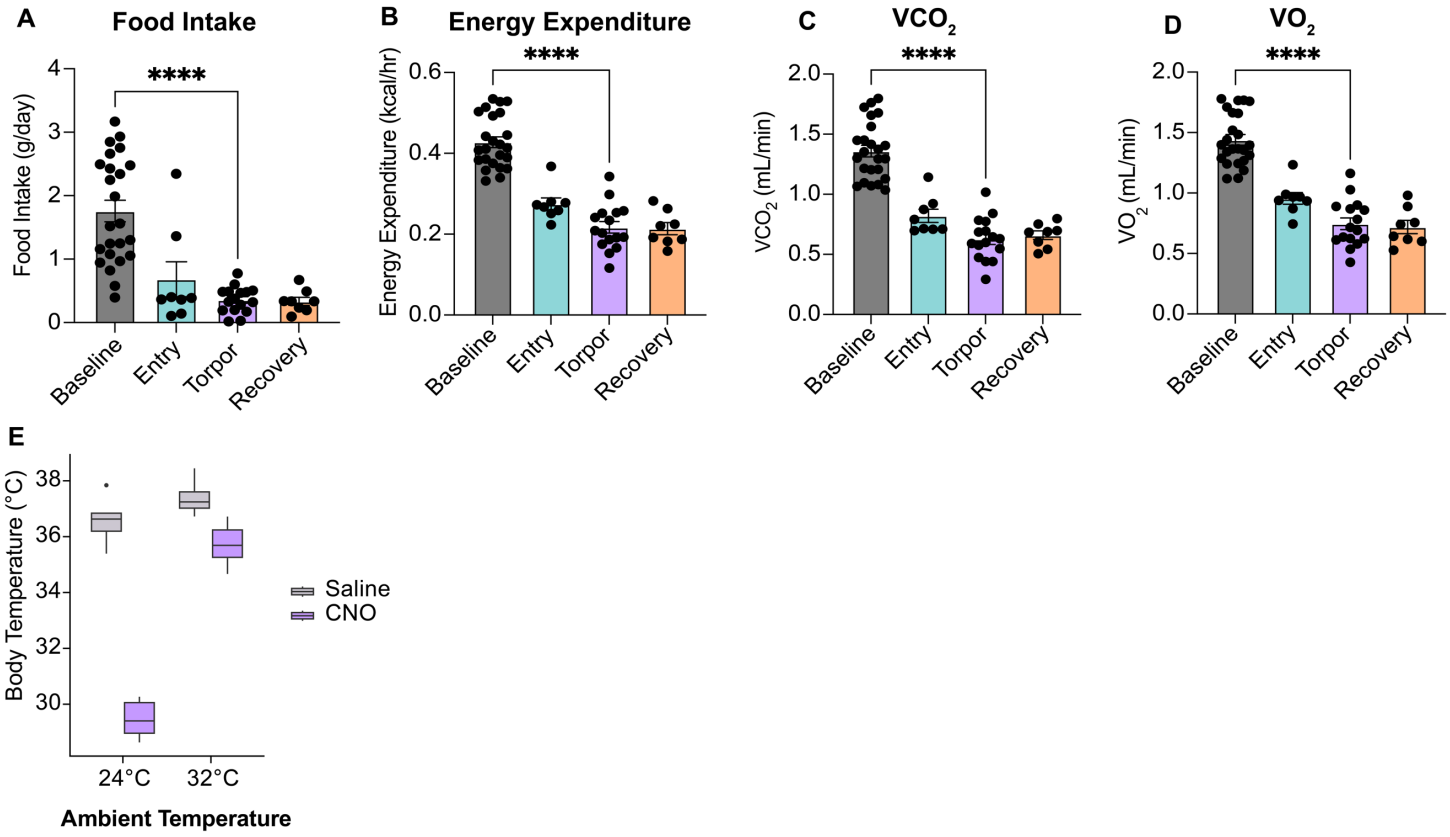

1190 **Supplementary Figure 1: avPOA stimulation regulates diverse metabolic parameters. (A-**
1191 **D**) Quantitation of (**A**) Food Intake, **(B)** Energy Expenditure, **(C)** VCO_2, and (**D**) VO_2
1192 throughout different phases of avPOA stimulation described in **Figures 1c-f**. Baseline = pre-
1193 CNO stimulation, Entry = 60 minutes post-CNO stimulation, Torpor = duration of torpor bout,
1194 Recovery = post-torpor period before returning to euthermia (**** = $p < 0.00005$, mean ±SEM,
1195 student's two-tailed t-test, n = 8 WT C57Bl/6J mice). **(E)** Quantitation of animal body
1196 temperature following 300 minutes of saline or Gq-DREADD stimulation at either T_a =24°C or
1197 32°C (n = 8, mean ±SEM).

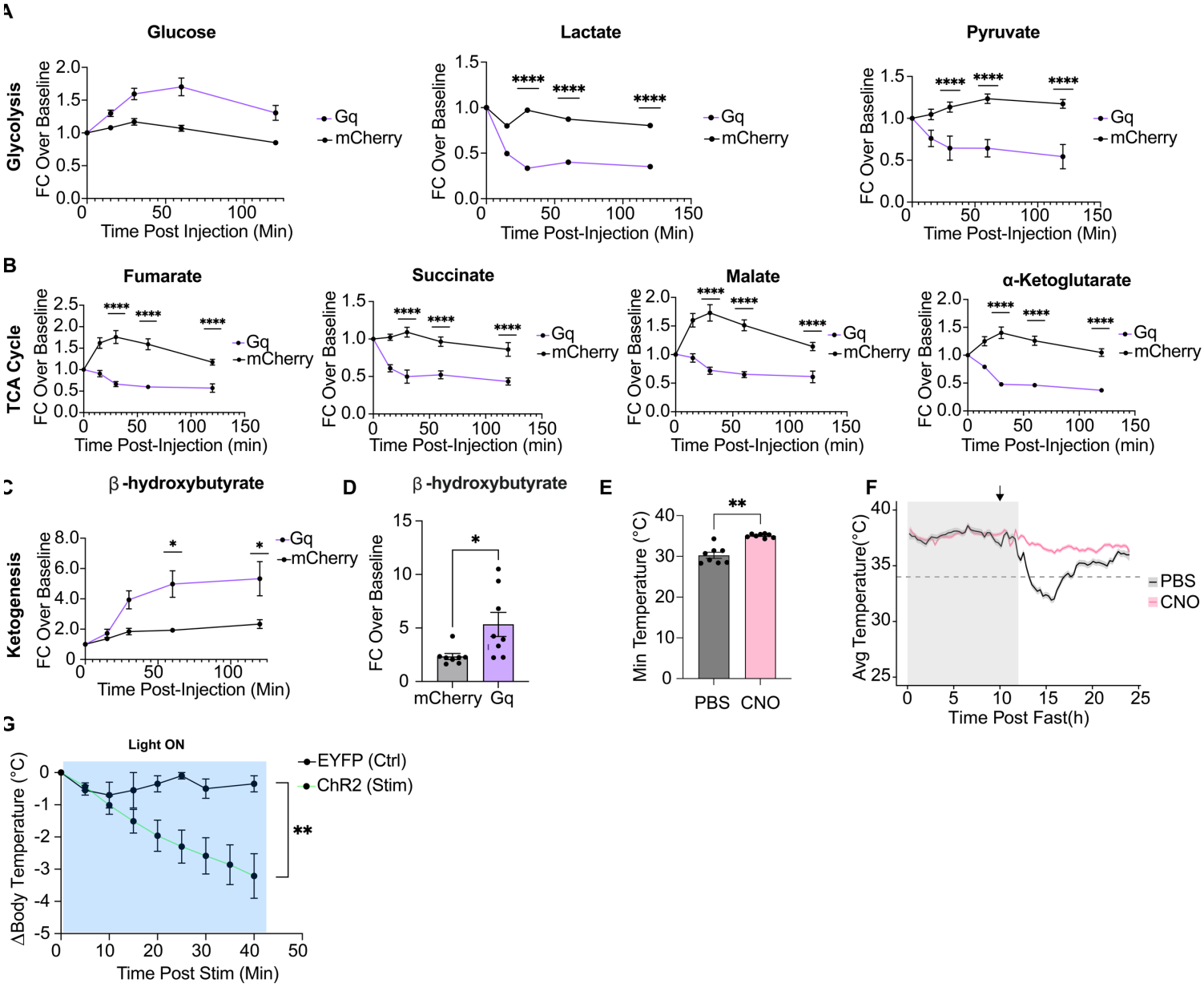

Supplementary Figure 2: TCA cycle and glycolytic metabolite abundance is altered following CNO stimulation. (A) Major glycolytic metabolites, including pyruvate and lactate, are monotonically decreased by CNO stimulation of Cre-dependent mCherry- or Gq-DREADD-transduced *Vglut2-IRES-Cre* mice as compared to their saline-injected counterparts. Conversely, glucose is monotonically increased upon CNO stimulation as compared to saline injection (** = $p < 0.005$, **** = $p < 0.00005$, student's two-tailed t-test, mean ±SEM, n = 8 animals). **(B)** Significantly downregulated TCA cycle metabolites include fumarate, succinate, malate, and α-ketoglutarate (**** = $p < 0.00005$, student's two-tailed t-test, mean ±SEM, n = 8 animals). Sample values reported as cohort-specific baseline-normalized fold change. Blood was collected

1207 at 0, 15, 30, 60, 120 minutes post-injection. **(C)** β-hydroxybuyrate levels are significantly
1208 increased in CNO-injected animals as compared to controls (* = $p < 0.05$, student's two-tailed t-
1209 test, mean ±SEM, n = 8 animals). **(D)** Quantitation of (C) 120 minutes after CNO stimulation in
1210 mCherry and Gq animals (* = $p < 0.05$, student's two-tailed t-test, mean ±SEM, n = 8 animals).
1211 **(E)** Quantification of minimal T_b measured during fasting-induced torpor in Gi-DREADD-
1212 transduced *Vglut2-IRES-Cre* animals. Animals were fasted for 24 hours at the beginning of the
1213 dark cycle (ZT 12), and either PBS or CNO (10 mg/kg) was injected 10 hours after fasting began
1214 (ZT 22) (** = $p < 0.005$, student's two tailed t-test, n = 8 PBS, n = 8 CNO, same animals, mean
1215 ±SEM). **(F)** Longitudinal trace of animals in (E), demonstrating that Gi-DREADD animals
1216 injected with CNO do not go into torpor due to inhibition of $avPOA^{Vglut2}$ neurons, whereas PBS-
1217 injected animals enter normally. Arrow corresponds to time of CNO or PBS injection. Gray
1218 shading indicates dark cycle (ZT12-24). Horizontal dashed line at 34.5°C corresponds to the
1219 temperature threshold for torpor entry. **(G)** Stimulation of $avPOA^{Vglut2}$ neurons with 455 nm light
1220 decreases body temperature in ChR2-, but not EYFP-expressing animals over the 40-minute time
1221 period of blue light stimulation (* = $p < 0.05$, student's two-tailed t-test, mean ±SEM, n = 4
1222 EYFP and n = 5 ChR2 animals).

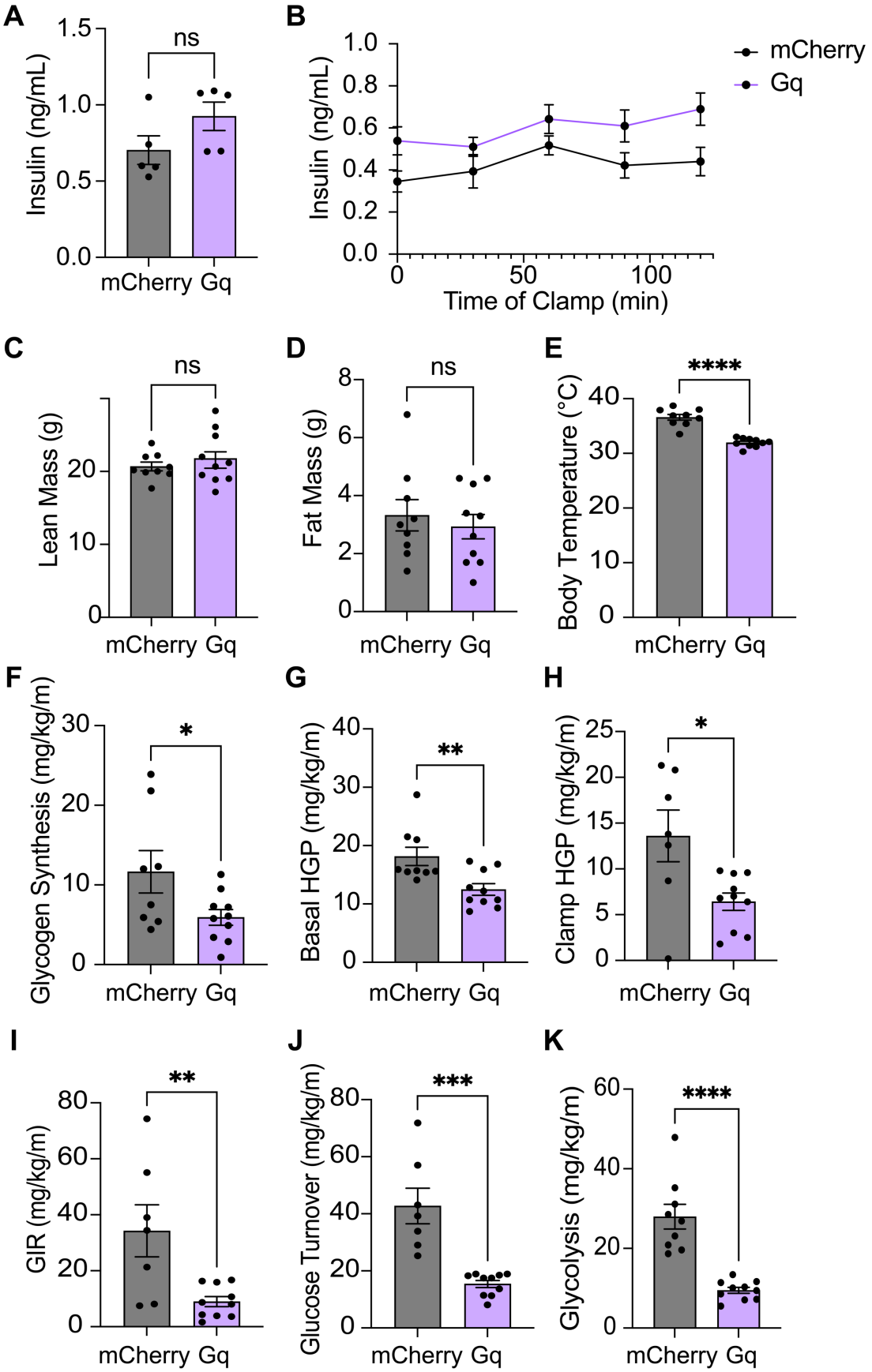
A
Insulin (ng/mL)
1.5
1.0
0.5
0.0
ns
mCherry Gq
B
Insulin (ng/mL)
1.0
0.8
0.6
0.4
0.2
0.0
0
50
100
Time of Clamp (min)
mCherry
Gq
C
Lean Mass (g)
ns
mCherry Gq
D
Fat Mass (g)
ns
mCherry Gq
E
Body Temperature (°C)
****
mCherry Gq
F
Glycogen Synthesis (mg/kg/m)
*
mCherry Gq
G
Basal HGP (mg/kg/m)
**
mCherry Gq
H
Clamp HGP (mg/kg/m)
*
mCherry Gq
I
GIR (mg/kg/m)
**
mCherry Gq
J
Glucose Turnover (mg/kg/m)
***
mCherry Gq
K
Glycolysis (mg/kg/m)
****
mCherry Gq

1223 **Supplementary Figure 3: Hyperinsulinemic-euglycemic clamp physical and clamp**
1224 **parameters. (A)** Quantification of glucose and insulin levels in plasma of fed *Vglut2-IRES-Cre*
1225 animals expressing Cre-dependent mCherry or Gq-DREADD in the avPOA, 60 minutes post-
1226 CNO injection ($p<0.005$ = **). **(B)** Hyperglycemic clamp experiment monitoring plasma insulin
1227 levels for 120 minutes during administration of various concentrations of glucose. Blood samples
1228 were taken at 0, 30-, 60-, 90-, and 120-minute time points throughout the experiment (n = 9
1229 mCherry, n = 10 Gq-DREADD animals). **(C-K)** correspond to the hyperinsulinemic-euglycemic
1230 clamp described in **Figure 3**. (**C)** Lean mass of animals analyzed by Dual X-ray Absorptiometry
1231 (DEXA) prior to beginning of the clamp. (**D)** Fat mass analyzed by DEXA prior to beginning of
1232 the clamp. (**E)** Average temperature of animals throughout the duration of the clamp. **(F)**
1233 Glycogen synthesis calculated during the clamp based on relative incorporation of ^{3}H into
1234 hepatic glycogen pool. (**G)** Hepatic Glucose Production (HGP) prior to initiation of the clamp as
1235 determined by the ratio of basal ^{3}H-Glucose infusion to the specific activity of plasma glucose
1236 prior to the initiation of the clamp. (**H)** Insulin-stimulated Hepatic Glucose Production during the
1237 clamp, determined by the difference between glucose infusion and whole-body glucose turnover
1238 rates. Insulin-stimulated HGP reflects the action of insulin on the liver specifically. **(I)** Glucose
1239 infusion rate (GIR) for each cohort. GIR was taken as an average over the duration of the
1240 experiment. Decreased GIR in Gq-DREADD-expressing animals indicates insulin insensitivity.
1241 Two control animals were excluded from analysis, as GIR measurements were highly irregular.
1242 **(J)** Glucose turnover in each cohort throughout the duration of the clamp, calculated as the ratio
1243 of ^{3}H-glucose infusion to plasma glucose specific activity during the final 30 minutes of the
1244 clamp. (**K)** Whole-body glycolysis estimated based on glycogen synthesis, GIR, and glucose
1245 clearance rates throughout the experiment (n = 9 mCherry, n = 10 Gq-DREADD, * = $p < 0.05$,
1246 ** = $p < 0.005$, *** = $p < 0.0005$, **** = $p < 0.00005$, two-tailed t-test).

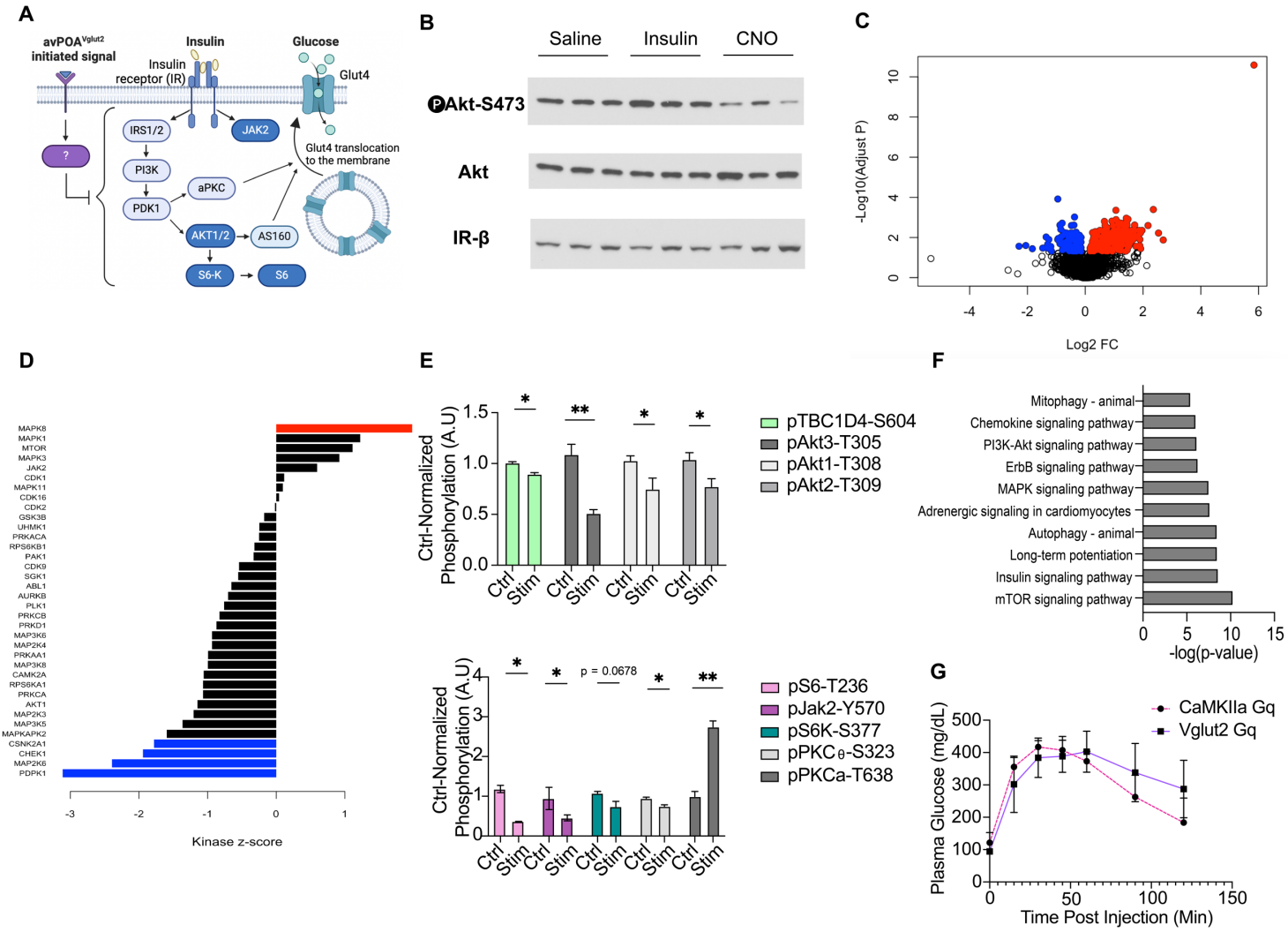

Supplementary Figure 4: Phosphoproteomic analysis of skeletal muscle reveals avPOA-induced defects in insulin signaling. (A) Schematic depicting the insulin signaling pathway and relevant downstream consequences of its activation with respect to glucose uptake. (**B)** Western blot of gastrocnemius muscle lysates obtained from mice injected with either saline, insulin, or CNO showing reduced Akt phosphorylation in CNO-injected animals as compared to saline-injected animals. **(C)** Volcano plot of differentially phosphorylated peptides in the gastrocnemius muscles of *Vglut2-IRES-Cre* mice transduced with Cre-dependent Gq-DREADD in the avPOA and injected with CNO as compared with saline. Significance threshold of $p < 0.05$ and Log_2FC of 0.6 used to determine significantly "hyperphosphorylated" or "hypophosphorylated" peptides. Red points correspond to peptides hyperphosphorylated in CNO relative to saline control, while blue correspond to hypophosphorylated peptides. **(D)** Kinase-substrate enrichment analysis score

1258 of various kinases identified within the dataset in CNO vs. saline control animals. Kinases whose
1259 substrates demonstrated hyperphosphorylation in CNO vs. saline control muscles were scored
1260 higher, and those that were significant are shown in red. Kinases whose substrates demonstrated
1261 hypophosphorylation in CNO vs. saline control were scored lower, and those that were
1262 significant are shown in blue. Z-score cutoff of |1.5| was used to determine significance. **(E)**
1263 Saline-normalized phosphorylation of individual residues in key proteins in the insulin signaling
1264 pathway (n = 3 animals per cohort, * = $p < 0.05$, ** = $p < 0.005$, student's two-tailed t-test). **(F)**
1265 GO-Term analysis of peptides that demonstrated significant ($p < 0.05$) hypophosphorylation in
1266 CNO vs. control animals. **(G)** Comparison of the efficiency of avPOA^{Vglut2} stimulation during a
1267 GTT using a CaMKIIa-Gq as compared with a DIO-Gq (AAV-hSyn1-DIO-hM3D(Gq)-
1268 mCherry) used in B6 and *Vglut2-IRES-Cre* animals, respectively. No statistically significant
1269 difference was observed between the two cohorts.

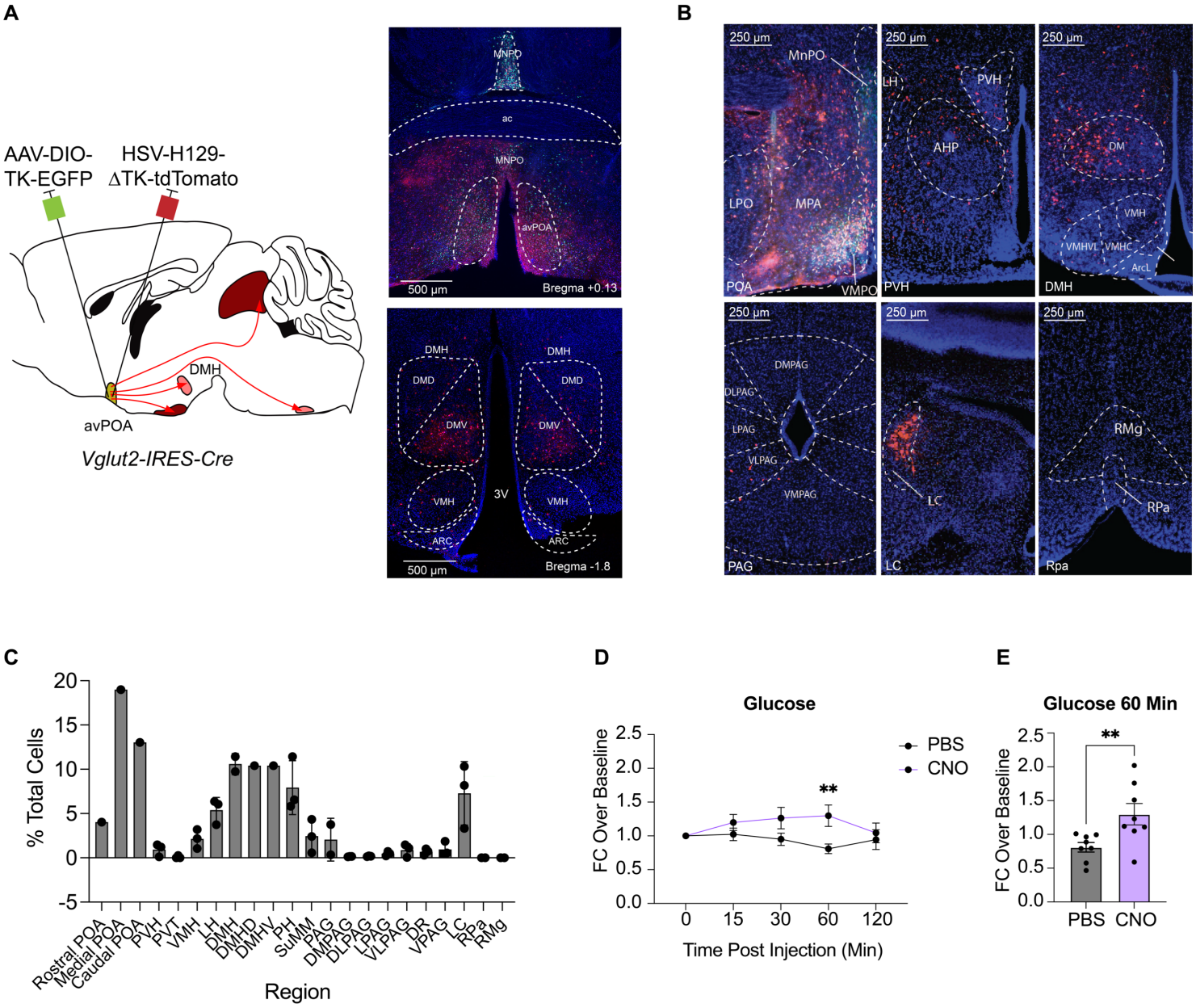
A
AAV-DIO-TK-EGFP
HSV-H129-ΔTK-tdTomato
DMH
avPOA
Vglut2-IRES-Cre
MNPO
ac
avPOA
500 µm
Bregma +0.13
DMH
DMD
DMV
VMH
ARC
3V
500 µm
Bregma -1.8
B
250 µm
MnPO
LH
PVH
AHP
LPO
MPA
POA
VMPO
DM
VMH
VMHVL
VMHC
ArcL
DMH
DMPAG
DLPAG
LPAG
VLPAG
VMPAG
PAG
LC
RMg
RPa
Rpa
C
% Total Cells
Region
Rostral POA
Medial POA
Caudal POA
PVH
PVT
VMH
LH
DMH
DMHD
DMHV
PH
SuMM
PAG
DMPAG
DLPAG
LPAG
VLPAG
DR
VPAG
LC
RPa
RMg
D
Glucose
FC Over Baseline
Time Post Injection (Min)
PBS
CNO
**
E
Glucose 60 Min
FC Over Baseline
PBS
CNO
**

1270 **Supplementary Figure 5: avPOA neurons project to diverse regions, which may have**
1271 **distinct effects on body temperature and blood glucose.** (**A**) (*Left*) Schematic for
1272 administration of AAV helper virus and HSV anterograde tracer to the avPOA of *Vglut2-IRES-*
1273 *Cre* animals. Mice were first transduced with a complementary helper AAV (AAV-DIO-TK-2A-
1274 EGFP), and after a two-week recovery period were transduced in the same region with HSV-
1275 H129-ΔTK-tdTomato, and sacrificed 65 hours following injection (n=3 *Vglut2-IRES-Cre*
1276 animals). (*Right*) (*Top*) Representative image of the starter region of the avPOA and (*Bottom*)
1277 one of the downstream targets of avPOA^{Vglut2} neurons in the dorsomedial hypothalamus (DMH).
1278 HSV^{+} cells labeled in red, AAV-DIO-TK-EGFP^{+} starter cells labeled in green. Note: in the
1279 DMH, HSV^{+} cells predominantly are observed in the ventral portion of the DMH (DMV). (**B)**
1280 Representative images of the same regions as **Figure 6a** in mice transduced with the anterograde
1281 monosynaptic tracer HSV-H129-ΔTK-tdTomato. (**C**) Quantitation of HSV expression in (B).
1282 Regions were defined in accordance with the Paxinos Reference Atlas, and the number of HSV-
1283 positive cells as a fraction of total DAPI cells was calculated for each region (n = 3 *Vglut2-IRES-*
1284 *Cre* animals, mean ±SEM). **(D)** Fold change in plasma glucose concentrations of *PACAP-2A-Cre*
1285 animals described in **Figure 6i** injected with either PBS or CNO at t = 0, 15, 30, 60, and 120
1286 minutes post-injection relative to baseline (** = $p < 0.005$, student's two tailed t-test, n = 8 PBS,
1287 n = 8 CNO, mean ±SEM). **(E)** Quantification of glucose levels of individual animals from (D) at
1288 t = 60 minutes post-injection (** = $p < 0.005$, student's two tailed t-test, n = 8 PBS, n = 8 CNO,
1289 mean ±SEM).

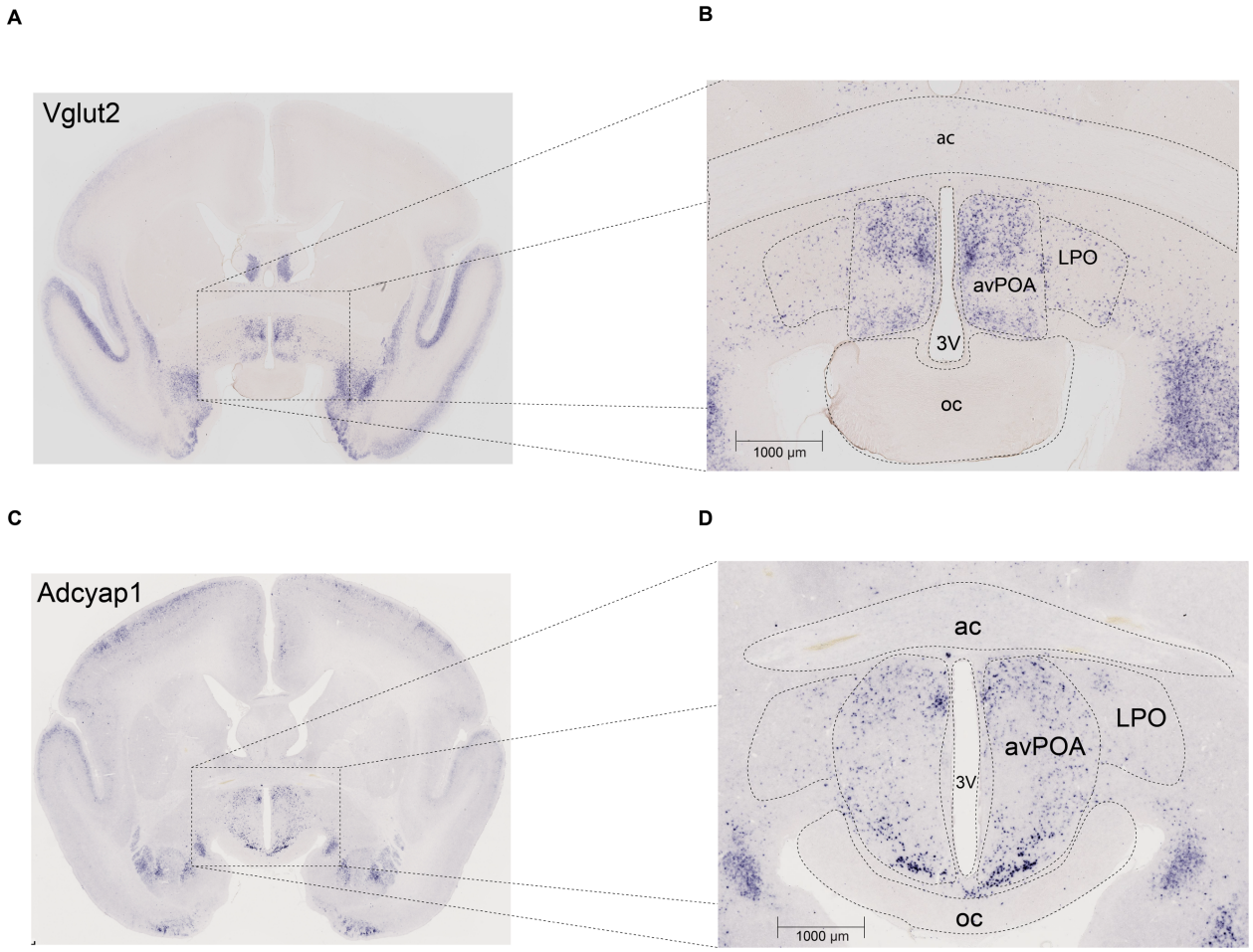

Supplementary Figure 6: avPOA expression of *Vglut2* and *Adcyap1* in the marmoset brain. **(A)** RNA fluorescence *in situ* hybridization (FISH) image of *Vglut2* RNA expression in coronal marmoset brain region corresponding to mouse avPOA. Purple puncta indicate *Vglut2* RNA expression. **(B)** Magnification of (A) to show the avPOA and LPO regions that correspond to the mouse brain, demonstrating that avPOA^{Vglut2} expression is anatomically conserved between species. **(C)** RNA FISH image of *Adcyap1* RNA expression in coronal marmoset brain region corresponding to mouse avPOA. Purple puncta indicate *Adcyap1* RNA expression. **(D)** Magnification of (C) to show the avPOA and LPO regions that correspond to the mouse brain, demonstrating that avPOA^{Adcyap1} expression is anatomically conserved between species. Images adapted from: https://gene-atlas.brainminds.jp/